J. Fluid Mech. (2021), *vol.* 926, A37, doi:10.1017/jfm.2021.757

Direct numerical simulation of inertio-elastic turbulent Taylor–Couette flow

Jiaxing Song[1], **Fenghui Lin**[1], **Nansheng Liu**[1],†, **Xi-Yun Lu**[1] **and**
Bamin Khomami[2],†

[1]Department of Modern Mechanics, University of Science and Technology of China, Hefei, Anhui 230026, PR China

[2]Department of Chemical and Biomolecular Engineering, University of Tennessee, Knoxville, TN 37996, USA

(Received 16 April 2021; revised 12 August 2021; accepted 19 August 2021)

The flow physics of inertio-elastic turbulent Taylor–Couette flow for a radius ratio of 0.5 in the Reynolds number (*Re*) range of 500 to 8000 is investigated via direct numerical simulation. It is shown that as *Re* is increased the turbulence dynamics can be subdivided into two distinct regimes: (i) a low $Re \leqslant 1000$ regime where the flow physics is essentially dominated by nonlinear elastic forces and the main contribution to transport and mixing of momentum, stress and energy comes from large-scale flow structures in the bulk region and (ii) a high $Re \geqslant 5000$ regime where inertial forces govern the flow physics and the flow dynamics is mainly governed by small-scale flow structures in the near-wall region. Flow–microstructure coupling analysis reveals that the elastic Görtler instability in the near-wall region is triggered via significant polymer extension and commensurately high hoop stresses. This instability gives rise to small-scale elastic vortical structures identified as elastic Görtler vortices which are present at all *Re* considered. In fact, these vortices develop herringbone streaks near the inner wall that have a longer average life span than their Newtonian counterparts due to their elastic origin. Examination of the budgets of mean streamwise enstrophy, mean kinetic energy, turbulent kinetic energy and Reynolds shear stress demonstrates that increasing fluid inertia hinders the generation of elastic stresses, leading to a monotonic reduction of the elastic-related effects on the flow physics.

Key words: turbulence simulation, viscoelasticity, Taylor–Couette flow

1. Introduction

Taylor–Couette (TC) flow, or flow between two concentric, independently rotating cylinders, is a classic paradigm for studies of nonlinear dynamics and hydrodynamic

---

† Email addresses for correspondence: lns@ustc.edu.cn, bkhomami@utk.edu

stability for both Newtonian and non-Newtonian fluids. Since the seminal work of Taylor (Taylor 1923), a tremendous number of studies have been focused on the transitions and instabilities of Newtonian fluids in the TC geometry with co-rotation or counter-rotation of the cylinders (Coles 1965; Andereck, Liu & Swinney 1986; Dutcher & Muller 2009*b*); in fact, many excellent reviews summarizing the results of these studies have been written (Swinney & Gollub 1985; Chossat & Iooss 1994; Fardin, Perge & Taberlet 2014; Grossmann, Lohse & Sun 2016). For a fixed outer cylinder, there are well-established sequences of transitions as the fluid inertia is enhanced. These transitions occur at a specific Reynolds number defined as $Re = \Omega R_i(R_o - R_i)/\nu$, where R_i and R_o denote the inner and outer cylinder radii, respectively, Ω is the inner cylinder angular velocity and ν represents the fluid kinematic viscosity. Specifically, as Re is progressively increased, the flow undergoes a series of transitions from a circular Couette flow, to an axially periodic Taylor vortex flow, and in turn to a state with waves superimposed on vortices and finally to chaotic and turbulent Taylor vortex flows (Coles 1965; Fernstermatcher, Swinney & Gollub 1979; Takeda 1999; Dutcher & Muller 2009*b*). When the flow becomes turbulent, small-scale streamwise-oriented, counter-rotating vortices, namely, Görtler vortices (GV) begin to emerge in the boundary layers over the concave or convex wall as a result of a Görtler instability (Barcilon *et al.* 1979; Barcilon & Brindley 1984; Wei *et al.* 1992; Saric 1994). Barcilon *et al.* (1979) hypothesized that the ‘herringbone shaped streaks’ observed in their experiments provided the evidence of GV occurring at the outer cylinder surface (Barcilon & Brindley 1984). This hypothesis was later critically examined by detailed experiments conducted by Wei *et al.* (1992) showing that the GV indeed exist and cause near-wall streaky structures to form the herringbone-like patterns. In fact, it was shown that the GV first emerge at the inner cylinder surface and then at the outer one, since the curvature and the velocity gradient are larger at the inner cylinder wall as compared with the outer one. These experimental observations were subsequently reproduced by Dong (2007) via direct numerical simulations (DNS) of turbulent TC flows at various Re. The simulations have further demonstrated that the GV appear first around the outflow boundaries between the large-scale Taylor vortices (TV) cells and then spread over the entire cylinder surface with increasing Re. In addition, the GV can result in stronger velocity fluctuations and give rise to streaky structures near the wall, which are known to play a significant role in the complex turbulent dynamics.

It is well known that the addition of a small amount of polymer to Newtonian fluids dramatically alters the instability and transitions reported for Newtonian fluids in the TC flow (Groisman & Steinberg 1996, 1997, 1998*a*,*b*; Muller 2008), where the elastic effect of the polymeric solution is commonly quantified by the Weissenberg number Wi, which is the product of the fluid relaxation time λ and the inverse of the characteristic shear rate of the flow, $\dot{\gamma}$ (Larson & Desai 2015). In the absence of fluid inertia ($Re \ll 1$), as Wi is increased, polymers become highly stretched along the curved streamlines and develop significant polymeric normal stresses, i.e. hoop stresses, that generate an elastic body force that squeezes fluid elements radially inward, rendering the flow linearly unstable; hence, this transition is of purely elastic origin (Larson, Shaqfeh & Muller 1990; Larson 1992; Sureshkumar, Beris & Avgousti 1994; Shaqfeh 1996; Groisman & Steinberg 1998*b*; Al-Mubaiyedh, Sureshkumar & Khomami 1999, 2000, 2002; Thomas, Sureshkumar & Khomami 2003; Ghanbari & Khomami 2014). This purely elastic instability through higher-order transitions can lead to the elastic turbulence (ET) state, which has completely different characteristics than the inertial turbulence (Groisman & Steinberg 2000, 2004; Steinberg 2021). ET displays large velocity fluctuations in a wide range of spatial and temporal scales with a power-law decay of the kinetic energy spectra in a frequency (f) domain $E(f) \sim f^{(-\alpha)}$, with the exponent $\alpha > 3$ (between -3.3 and -3.6 depending on the flow geometry) (Fouxon & Lebedev 2003; Groisman & Steinberg 2004; Steinberg 2019). Thus, due to the steep decay of the velocity spectrum, ET is essentially a spatially smooth and temporally random flow, dominated by strong nonlinear interaction of a few large-scale spatial modes (Steinberg 2021).

When both fluid inertia (Re) and elasticity (Wi) are sufficiently high (typically $1 < Re \leqslant 10^3$), the elasticity number, $El = Wi/Re$ is commonly used to evaluate the relative importance of elastic and inertial effects (Avgousti & Beris 1993; Baumert & Muller 1995). In the range of very low elasticity ($El \ll 1$), researchers have primarily recovered transitions similar to Newtonian fluids, with the critical thresholds shifted slightly due to the presence of a small amount of fluid elasticity (Groisman & Steinberg 1998*b*; Crumeyrolle & Mutabazi 2002; Dutcher & Muller 2009*a*, 2011; Mohammadigoushki & Muller 2017). While in the presence of moderate elasticity ($El \sim 10^{-2}$), the transitions observed for Newtonian fluids are modified by elasticity and replaced by new transition sequences involving highly localized flow patterns such as rotating standing waves (RSW), disordered oscillations, oscillatory strips and diwhirls (similar to the ‘flame pattern’ observed by Baumert & Muller 1997, 1999) (Groisman & Steinberg 1996, 1997, 1998*a*,*b*; Crumeyrolle & Mutabazi 2002; Muller 2008). The aforementioned flow patterns and transition pathways have been faithfully reproduced via high-fidelity DNS with $El = 1/3$ by using the FENE-P (finitely extensible nonlinear elastic-Peterlin) viscoelastic model (Bird *et al.* 1987) that mimics the rheological properties of dilute polymer solutions used in the experiments (Thomas, Khomami & Sureshkumar 2006*b*, 2009).

More recently, Dutcher & Muller (2009*a*, 2013) reported a different series of transitions for a slightly shear-thinning polyethylene oxide solution at $0.1 < El < 0.2$. Specifically, the following transition sequence was observed: From the azimuthal flow to standing vortices, followed by disordered RSW and then to a turbulent-like TC flow labelled elasticity-dominated turbulence (EDT), accompanied by a transition hysteresis. Latrache, Crumeyrolle & Mutabazi (2012) have also identified two regimes of turbulence in the viscoelastic TC flows of shear-thinning polyethylene oxide–alcohol–water solution for $0.01 \leqslant El \leqslant 0.05$, namely, spatio-temporal intermittency and inertio-elastic turbulence. Elastically induced turbulent flows have also been realized numerically by our previous DNS at $0.2 \leqslant El \leqslant 5$ (Liu & Khomami 2013*a*). The simulations have shown the coexistence of highly localized elastically driven inflows (along the axis of the cylinder similar to the solitary coherent structures such as oscillatory strips and diwhirls) and centrifugally driven outflows, clearly underscoring the strong competition between fluid inertia and polymer induced elastic forces in this class of flows.

Although the aforementioned studies of turbulent flows in the inertio-elastic regime have identified new and unique transition scenarios, the lack of experimental techniques to precisely measure the elastic stress fields in this class of flows has prevented complete experimental characterization of the flow structures and the underlying polymer induced and/or modified turbulent dynamics. Thus, a fundamental question arises, namely, how do inertial effects modify flow structures and turbulence dynamics as well as the flow microstructure coupling in the inertio-elastic turbulence of curvilinear flows such as TC flow where the hoop stresses play a central role in driving flow transition and nonlinear dynamics? Some preliminary work in this direction has been performed. Specifically, Lee, Sengupta & Wei (1995) conducted a series of experiments at $1500 \leqslant Re \leqslant 30\,000$ to study the effect of polymer additives on the near-wall structures of turbulent TC flow. They demonstrated that polymer additives have a stabilizing effect on near-wall centrifugal instabilities, i.e. the GV formation was suppressed. In addition, it was shown that the measured Görtler instability wavelength decreases with increasing Re and with decreasing polymer concentration. In addition, Liu & Khomami (2013*b*) have performed extensive DNS of high-*Re* ($Re = 5000$) viscoelastic turbulent TC flows and revealed the occurrence of inertio-elastic Görtler instability near the outer wall and the breakdown of large-scale Newtonian TV that results in significant drag enhancement. Moreover, the drag enhancement mechanism in viscoelastic turbulent TC flow shows a strong curvature dependence, namely, for a small radius ratio $\eta = R_i/R_o$ the large-scale TV are destabilized by an elastic/inertio-elastic Görtler instability near the inner/outer wall; while for a large radius ratio η the well-organized TV occupying the entire gap persist due to the stabilizing effects of elasticity (Song *et al.* 2019).

In contrast, the addition of minute amounts of long chain polymers to rectilinear (unidirectional) wall-bounded turbulence leads to a dramatic decrease in turbulent friction drag, which saturates at $\sim$80 % reduction, the so-called maximum drag reduction asymptote (Toms 1948; Lumley 1969; Virk 1975). The origin of polymer-induced drag reduction has been ascribed to polymer stretch in the near-wall region that acts to suppress the self-sustaining process of wall turbulence, as evinced by the weakened near-wall vortices of larger length scale (Lumley 1977; Metzner 1977; Sureshkumar, Beris & Avgousti 1997; Li, Sureshkumar & Khomami 2006; Kim *et al.* 2007; White & Mungal 2008; Li, Sureshkumar & Khomami 2015; Teng *et al.* 2018; Marchioli & Campolo 2021). Samanta *et al.* (2013) have proposed that the maximum drag reduction dynamics is driven by an elasto-inertial instability that can even eliminate the Newtonian turbulence. Hence, the maximum drag reduction state can be interpreted as a self-sustained elasto-inertial turbulence (EIT), where the turbulence is sustained mainly by the fluctuations of small-scale elastic structures (Dubief, Terrapon & Soria 2013; Sid, Terrapon & Dubief 2018). Recent studies in pipe (Choueiri, Lopez & Hof 2018; Lopez, Choueiri & Hof 2019) and channel (Shekar *et al.* 2019) flows have provided convincing evidence that a reverse transition pathway from Newtonian turbulence via a relaminarization of the flow can eventually lead to the EIT state. An important advancement towards understanding the EIT dynamics has been achieved recently by Shekar *et al.* (2019, 2020). Specifically, they have shown that the trains of weak spanwise-oriented flow structures with inclined sheets of polymer stretch are related to a new viscoelastic nonlinear Tollmien–Schlichting attractor, that is nonlinearly sustained by viscoelastic stresses. However, small-scale elastic structures display streamwise-oriented flow topology in the viscoelastic TC turbulence, leaving the underlying elasticity-driven physics, in particular the role of hoop stresses in generation of turbulence and vortical structures, an open question.

It is well known that inertia plays a very important role in flow transitions, pattern formation, turbulence dynamics and drag modification of viscoelastic TC flow. To this end, to provide a clear mechanistic understanding of how variation in *Re* affects flow transitions in the viscoelastic TC flow, we have examined the flow dynamics over a broad range of *Re* while keeping the *Wi* constant. Although it is much more difficult to experimentally realize the inertially driven flow transitions obtained by the present simulations, the desired mechanistic understanding of flow transitions from an elastically dominated to an inertio-elastic, and finally to an inertially dominated turbulent flow can only be readily obtained via the strategy employed in this study. The present work is dedicated to examining the influence of fluid inertia on the flow structure and the turbulence dynamics of viscoelastic turbulent TC flow in the inertio-elastic regime. To this end, we have performed DNS for a radius ratio $\eta = 0.5$ at five Reynolds numbers, ranging from 500 to 8000, corresponding to low to moderate *El* in the range of $0.00375 \sim 0.06$. Specifically, we depict how the increase in Reynolds number leads to the flow transitions from EDT to inertia-dominated turbulence (IDT), highlighted by striking changes in the near-wall herringbone streaks as well as statistical quantities.

2. Problem formulation and computational details

2.1. *Governing equations*

In our prior studies we have successfully used a fully spectral, three-dimensional parallel algorithm to predict high-order nonlinear viscoelastic TC flow transitions (Thomas *et al.* 2006*a*,*b*, 2009) and study viscoelastic TC turbulence (Liu & Khomami 2013*a*,*b*; Song *et al.* 2019). In this study, we have used a modified version of this code to avoid use of artificial diffusion (AD) to stabilize numerical integration of the conformation tensor evolution equation (see below for details). Similar to our prior studies, the FENE-P constitutive equation is used to model the polymer contribution to the total stress. The physical connection of the FENE-P model to real elastic liquids, i.e. dilute solutions of high molecular weight, finitely extensible flexible polymers in a theta solvent, makes it a model of choice for this class of simulations. This model captures the essential rheological response of this class of fluids both in shear and extension. The maximum chain extensibility is defined as L, and remains constant in the simulations. Thus, flow-induced polymer chain scission is not captured in our simulations. Overall, chain scission in stochastic flows has not been extensively studied; even if a model existed that could accurately capture flow-induced chain scission in this class of flows, its implementation in DNS of viscoelastic flows would require computational power well beyond today's most advanced supercomputers. We have chosen $d = R_o - R_i$, $d/\varOmega R_i$, $\varOmega R_i$, $\rho(\varOmega R_i)^2$ and $\eta_p \varOmega R_i/d$ as scales for length, time, velocity $\boldsymbol{u}$, pressure p and polymer stress $\boldsymbol{\tau}$, respectively. Here, ρ represents the solution density, and the total zero-shear solution viscosity η_t is the sum of the solvent (η_s) and polymeric (η_p) contributions. Further, we scale the conformation tensor $\boldsymbol{C}$, which represents the ensemble average of the second moment of the end-to-end vector of the polymer chain, with respect to BT/H, where B, T and H denote the Boltzmann constant, absolute temperature and the Hookean spring constant of the elastic dumbbell model, respectively. The resulting dimensionless equations governing the motion of an incompressible FENE-P fluid are as follows:

$$\nabla \cdot \boldsymbol{u} = 0, \tag{2.1}$$

$$\frac{\partial \boldsymbol{u}}{\partial t} + \boldsymbol{u} \cdot \nabla \boldsymbol{u} = -\nabla P + \frac{\beta}{Re}\nabla^2 \boldsymbol{u} + \frac{1-\beta}{Re}\nabla \cdot \boldsymbol{\tau}, \tag{2.2}$$

and

$$\frac{\partial \boldsymbol{C}}{\partial t} + \boldsymbol{u} \cdot \nabla \boldsymbol{C} = \boldsymbol{C} \cdot \nabla \boldsymbol{u} + (\nabla \boldsymbol{u})^{\mathrm{T}} \cdot \boldsymbol{C} - \boldsymbol{\tau}, \tag{2.3}$$

where polymer molecules are modelled as dumbbells composed of two beads and a nonlinear spring, and the polymer stress $\boldsymbol{\tau}$ can be related to the stress conformation tensor $\boldsymbol{C}$ via the relationship

$$\boldsymbol{\tau} = \frac{f(\boldsymbol{C})\boldsymbol{C} - \boldsymbol{I}}{Wi}. \tag{2.4}$$

The function $f(\boldsymbol{C})$, known as the Peterlin function, is defined as

$$f(\boldsymbol{C}) = \frac{L^2 - 3}{L^2 - \mathrm{trace}(\boldsymbol{C})}. \tag{2.5}$$

In the above equations, $\beta = \eta_s/\eta_t$ is the solvent to total viscosity ratio; the Reynolds number is defined as $Re = \rho \varOmega R_i d/\eta_t$, and the Weissenberg number as $Wi = \lambda R_i \varOmega/d$. The velocity vector $\boldsymbol{u}$ is composed of three components u_r, u_θ and u_z in the r, θ and z directions, respectively, in a cylindrical coordinate system, where the z-axis coincides with the cylinder axis. The length of the computational domain along the cylinder axis is set as $L_z = \pi d$, so the effects of large-scale TV in the gap and turbulent fluctuations can be obtained reliably (Ostilla-Mónico, Verzicco & Lohse 2015). The governing equations are also supplemented by no-slip boundary conditions at the walls, as well as periodic boundary conditions in the z direction.

2.2. *Numerical method*

The hyperbolic nature of polymer conformation tensor evolution equation requires special consideration to ensure numerical convergence especially at high *Wi* (Alves, Oliveira & Pinho 2021). Adding a global AD term $\kappa\nabla^2\boldsymbol{C}$ to this equation is a common and successful practice for attaining numerical stability in inertially dominated turbulent flows (Sureshkumar, Beris & Avgousti 1995; Sureshkumar *et al.* 1997; Li *et al.* 2006). To ensure accuracy of the solution in the presence of AD, extensive studies have been performed where the influence of Schmidt number $Sc[= (Re\kappa)^{-1}]$ on the overall flow dynamics has been studied (Gupta & Vincenzi 2019; Zhu & Xi 2020). Specifically, it has been shown that a small diffusivity $[Sc \sim O(10^{-1})]$ will not modify the essential features of the velocity and polymer conformation tensor fields in inertially dominated turbulent flows. However, the presence of AD has recently been linked to the inability of simulations to resolve small-scale elastic structures and this has been identified as the main reason for inability of many prior studies to observe the elasto-inertial instability in channel flows (Sid *et al.* 2018).

The use of local or global AD in viscoelastic flow simulation has been a subject of debate for decades (Talwar, Ganpule & Khomami 1994; Alves *et al.* 2021). Specifically, it has been shown that convergent and accurate solutions can be obtained when the convective term in the conformation tensor evolution equation is discretized using techniques appropriate for hyperbolic equations (Vaithianathan *et al.* 2006). To this end, in this study we have used a proven technique (Zhu & Xi 2020), namely, a pseudo-spectral/finite-difference hybrid method (HM) to simulate the viscoelastic TC flow. Specifically, the convective term in the conformation tensor evolution equation (2.3) is discretized with a second-order conservative total variation diminishing finite-difference scheme with the MINMOD limiter (Yu & Kawaguchi 2004); a pseudo-spectral method (SM) discretization is used for all other terms, which maximally preserves accuracy and efficiency. In addition, a semi-implicit second-order predictor–corrector Adams–Bashforth scheme is used for time integration of the conformation tensor equations (Housiadas & Beris 2004), where the linear stress relaxation term is treated implicitly to strictly enforce the chain finite maximum extension limit (Vaithianathan & Collins 2003; Dubief *et al.* 2005). As expected, for all the parameters studied here, this algorithm is numerically stable and preserves the positive definiteness as well as the boundedness of the polymer conformation tensor ($0 < \mathrm{trace}(\boldsymbol{C}) < L^2$).

2.3. *Code assessment*

In order to demonstrate the accuracy of our HM code, a multi-step hierarchical validation strategy has been adopted: (i) comparison with analytical solution of laminar flow, (ii) faithfully capturing a unique flow pattern in viscoelastic TC flow, namely, ribbon or RSW flow (Groisman & Steinberg 1996, 1998*a*; Thomas *et al.* 2009) and (iii) the inertio-elastic turbulent flow. In the present study, $\langle\,\rangle = \langle\langle\langle\,\rangle_\theta\rangle_z\rangle_t$, denotes hereafter averaging in the θ-direction ($\langle\,\rangle_\theta$), the z-direction ($\langle\,\rangle_z$) and time ($\langle\,\rangle_t$), and the fluctuating

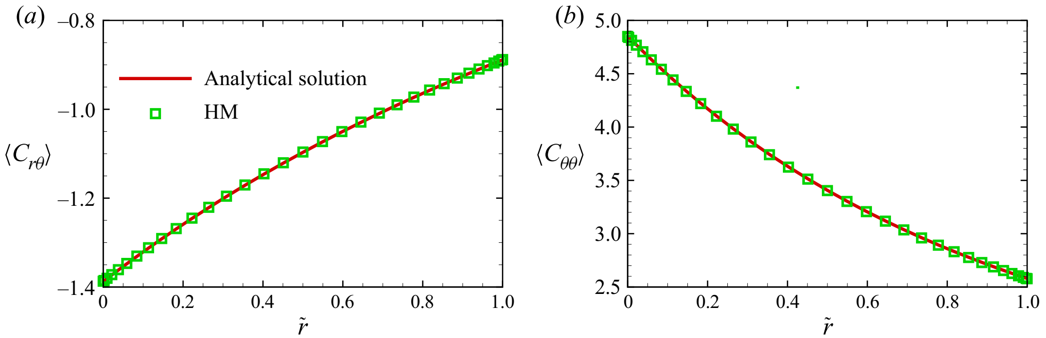

Figure 1. Profiles of (*a*) mean conformation component $\langle C_{r\theta}\rangle$ and (*b*) $\langle C_{\theta\theta}\rangle$ obtained by analytical solution and HM simulation at $Re = 40$, $Wi = 1$, $L = 100$, $\beta = 0.8$.

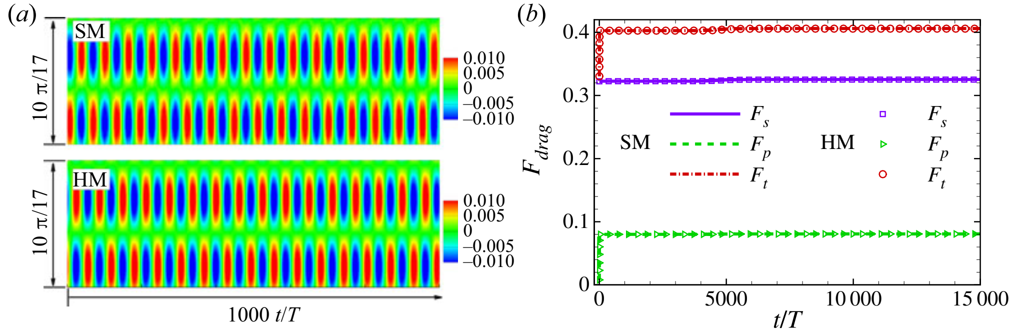

Figure 2. (*a*) Space–time plots of radial velocity u_r along the axial line positioned at $r = (R_i + R_o)/2$ and $\theta = \pi$ showing flow states calculated by SM and HM methods at $Re = 86.6$, $Wi = 4.33$, $L = 100$, $\beta = 0.8$. (*b*) Time series of drag forces at the inner cylinder wall. Here, total drag forces F_t is the sum of solvent F_s and polymer F_p contributions, $F_s = 2\beta\int_0^{L_z} \mathrm{d}z \int_0^{2\pi} S_{r\theta}\, r\, \mathrm{d}\theta/Re/L_z$, $F_p = (1-\beta)\int_0^{L_z} \mathrm{d}z \int_0^{2\pi} \tau_{r\theta}\, r\, \mathrm{d}\theta/Re/L_z$, where $S_{r\theta}$ is the (r, θ) component of the velocity gradient tensor $\boldsymbol{S} = (\nabla \boldsymbol{u} + (\nabla \boldsymbol{u})^{\mathrm{T}})/2$.

part of variable v is obtained as $v' = v - \langle v\rangle$. In addition, $\tilde{r} = (r - R_i)/d$ is the dimensionless distance to the inner cylinder wall.

A comparison of the HM numerical results with the analytical solutions of laminar viscoelastic TC flow is depicted in figure 1. The simulation parameters correspond to a laminar Couette flow with parameters extracted from linear stability analysis results (Thomas 2006). Specifically, the simulation is performed at $Re = 40$, $Wi = 1$ with $L = 100$, $\beta = 0.8$ with a unit tensor as the initial condition for the conformation tensor; the mean tangential ($\langle C_{r\theta}\rangle$) and normal ($\langle C_{\theta\theta}\rangle$) components of the conformation tensor obtained by HM are in excellent agreement with the analytical solution.

A ribbon flow state simulated by HM and SM without use of AD has also been examined. The ribbon patterns obtained by the two methods shown in figure 2(*a*) are indistinguishable; their checkerboard-like features signifying the expected alternative regions of radial inflow (blue) and outflow (red) are accurately captured (Groisman & Steinberg 1996, 1998*a*; Thomas *et al.* 2009). The time periods associated with the fluctuating radial velocity in the ribbons are approximately 14.45λ and 14.62λ for SM and HM, respectively. Moreover, in figure 2(*b*), the time series of total drag force (F_t) and its components of Newtonian viscous shear stress (F_s) and elastic shear stress (F_p) obtained by these two methods show good agreements with relative error less than 0.06 %.

Finally, a comparison between the results of the high-*Re* viscoelastic TC turbulence simulated by previously developed SM and the new HM is made. Due to the aforementioned numerical stability problem, a global AD term is added to the SM for simulation of dilute polymer solution at $\beta = 0.9$ and large extensibility $L = 100$ at $Re = 3000$, $Wi = 30$. Thus, the validation in this part can also be viewed as a critical examination of the effects of AD on the flow structure and the turbulence statistics in the elasto-inertial turbulent TC flow. The profiles of mean velocity $\langle u_\theta \rangle$ and polymer shear stress $\langle \tau_{r\theta} \rangle$ are shown in figure 3(*a*,*b*). Excellent agreements between the computed velocity and shear stress profiles are observed, particularly at high *Sc*. Furthermore, the profiles of fluctuations in velocity and elastic shear stress depicted in figure 3(*c*,*d*) shows minor differences between the two schemes at high *Sc*. The modifications of flow structures can be further quantified by the differences in the one-dimensional spanwise spectra of the turbulent kinetic energy (TKE) and polymer stretch for different *Sc* (see figure 4). The energy in the high-wavenumber regime is lower for the SM results of finite S_c than that obtained by the HM technique. However, in the low-wavenumber regime, the profiles collapse indicating the large-scale flow structures remain nearly unchanged for the range of S_c considered. To this end, these comparisons taken together have revealed that the HM code can faithfully reproduce high-*Re* viscoelastic TC turbulence flow features and statistics (Liu & Khomami 2013*b*; Song *et al.* 2019). At the same time, the *Sc* sensitivity analysis suggests that $Sc \sim O(1)$ can capture the essential features of the velocity and polymer stress fields in high-*Re* viscoelastic TC simulations. However, it should be noted that the addition of the AD term mainly modifies/reduces the large polymer stress gradients in the flow field that give rise to small-scale structures as evinced by the small-scale elastic GV formed near the inner cylinder walls where large stress gradients exist (Song *et al.* 2019). To this end, addition of AD mainly affects/dissipates small-scale elastic flow structures (see figure 4). This is consistent with the previous findings regarding the influence of AD on simulations of inertia-driven and elasto-inertial viscoelastic turbulence (Sid *et al.* 2018; Gupta & Vincenzi 2019; Zhu & Xi 2020). Based on our earlier studies of the curvature dependence of viscoelastic TC turbulence (Song *et al.* 2019), decreasing the gap (larger η) is expected to lead to weakening and elimination of the small-scale elastic GV, due to the fact that elastic effects are more significant at smaller η. That is, a decrease in η leads to an increase in curvature and commensurately higher hoop stresses (Larson *et al.* 1990; Groisman & Steinberg 1998*b*). Thus the AD effect is more prominent near the walls where significant polymer stretch is realized due to the mean-flow shear. This in turn, leads to larger polymer stress gradients and formation of an elastic boundary layer. Evidently, the AD effect is more pronounced in small gap systems.

It should be noted that figure 3(*c*,*d*) depicts that the most accurate results correspond to those of the full pseudo-spectral calculation with the highest $Sc = 3.33$. Evidently, the predictions of the HM technique fall between the spectral results obtained with two different global AD values. This underscores the fact that introduction of a low-order upwind finite-difference approximation for the convection term introduces numerical diffusion mainly in the radial direction. However, the scheme does produce results that are very similar to fully spectral techniques with small global AD of $Sc \sim O(1)$. In addition, it ensures positive definiteness of the conformation tensor and the hyperbolic-like nature of the constitutive equation. Hence, if SM with sufficiently high-order approximating function and $Sc \sim O(1)$ is coupled with available schemes that ensure positive definiteness of the conformation tensor (Housiadas, Wang & Beris 2010), reliable results can be obtained. To this end, the HM technique used in this study can be viewed as an equivalent technique to traditional SM with a sufficiently high *Sc* value.

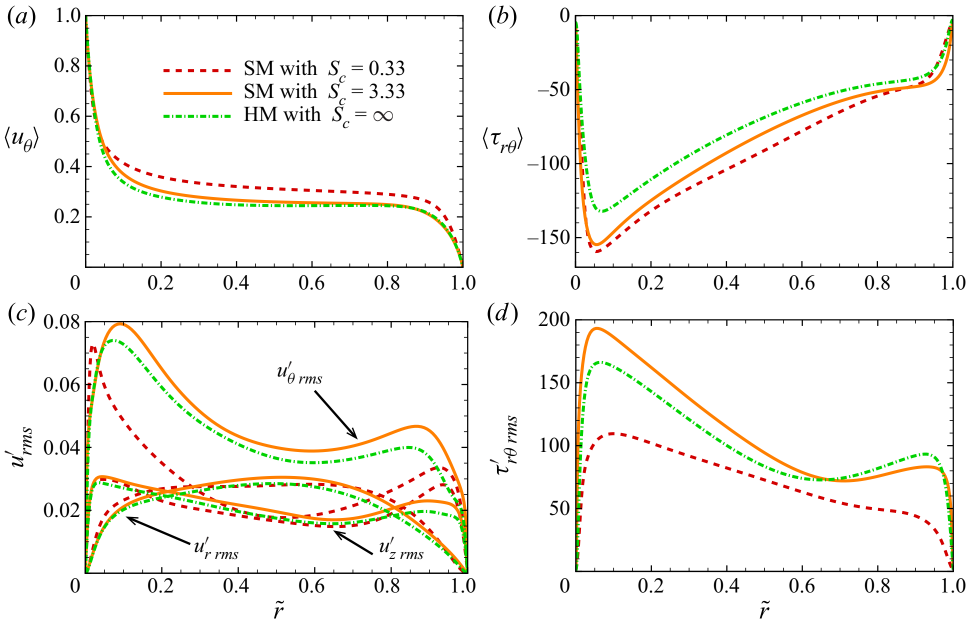

Figure 3. Profiles of (*a*) mean azimuthal velocity $\langle u_\theta \rangle$ and (*b*) mean polymer shear stress component $\langle \tau_{r\theta} \rangle$, (*c*) root-mean-square (r.m.s.) values of three velocity components and (*d*) polymer stress component $\tau_{r\theta}$ at $Re = 3000$, $Wi = 30$, $L = 100$ with various Sc.

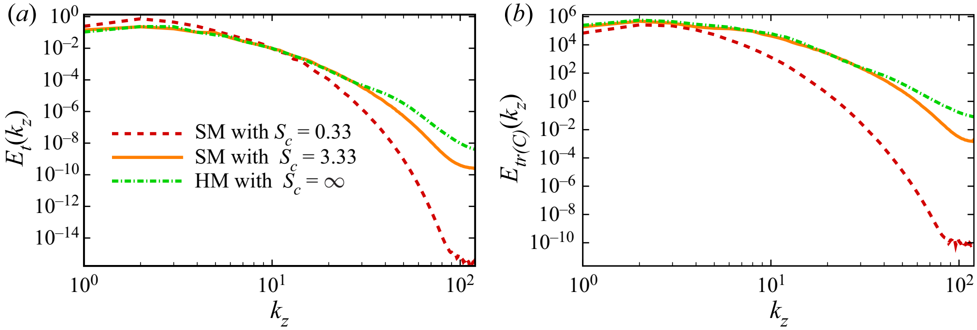

Figure 4. One-dimensional spectra of the turbulent kinetic energy ($\langle \boldsymbol{u}' \cdot \boldsymbol{u}' \rangle/2$) (*a*) and polymer stretching ($\langle \mathrm{tr}(\boldsymbol{C}) \rangle$) (*b*) sampled at the middle of the gap for viscoelastic flows of $Re = 3000$, $Wi = 30$, $L = 100$ with various Sc.

2.4. *Simulation parameters*

The viscoelastic TC flow of a dilute long chain polymer solution with $\beta = 0.9$ and $L = 100$, at $Wi = 30$ is investigated in the Reynolds number range of 500 to 8000 to scrutinize the influence of fluid inertia on the inertio-elastic turbulent flow structures and statistics. This corresponds to El in the range of $0.00375 \sim 0.06$. All the simulations are started from a fully developed inertio-elastic turbulent flow at $Re = 3000$, $Wi = 30$ with radius ratio $\eta = R_i/R_o = 0.5$. Based on this flow field, we decrease the Reynolds number to 1000, 500 to obtain results for the low-Re regime and increase it to 5000, 8000 for the high-Re regime. Simulation parameters and the grid resolutions are summarized in table 1.

Re	$N_r \times N_\theta \times N_z$	Δr^+	$r\Delta\theta^+$	Δz^+	δ_τ	Re_τ
500	128 × 128 × 256	0.11–0.88	3.51	0.88	0.0140	69.70
1000	128 × 128 × 256	0.17–1.41	5.64	1.41	0.0087	115.12
3000	128 × 128 × 256	0.38–3.07	12.27	3.07	0.0040	250.61
5000	128 × 256 × 512	0.56–4.54	9.09	2.27	0.0027	373.54
8000	128 × 256 × 512	0.79–6.46	12.92	3.23	0.0019	518.83

Table 1. Numerical parameters and grid resolutions. The superscript '+' is used to denote the quantities non-dimensionalized by the viscous length scale $\delta_\tau = \eta_t/\rho/u_\tau$; the friction velocity is defined as $u_\tau = \sqrt{\tau_w/\rho}$, where τ_w is the total wall stress; the friction Reynolds number is defined as $Re_\tau = \rho u_\tau d/\eta_t$.

As Gauss–Lobatto–Chebyshev polynomials are applied in the wall normal (r-) direction and Fourier series in the periodic (θ- and z-) directions, mesh grids are clustered near the inner and outer walls in the r-direction, and uniform in the θ- and z-directions. The time scale is made dimensionless by the convective time unit, $T = d/(\varOmega R_1)$. Sufficiently long simulations (at least $300T = 10\lambda$) have been performed to ensure that statistically steady flow states are realized. To evaluate the turbulence statistics, ensemble averaging is performed for time periods of approximately $120T$.

3. Small-scale elastic GV

In this section, the flow structures in turbulent TC flow with particular emphasis on small-scale GV near the inner cylinder wall are discussed in detail. Similar to our previous findings in the viscoelastic turbulent TC flow at this radius ratio (Liu & Khomami 2013*b*; Song *et al.* 2019), the well-organized large-scale TV identified in the Newtonian flow are no longer observed in the time and θ-direction averaged flow fields at all Re considered (see figure 5*a*). Instead, a large number of vortices span across the entire gap. Also, the GV are smaller in size and higher in number near the inner wall. The instantaneous flow fields depicted in figure 5(*b*), show that increasing Re leads to a monotonic increase in number of the vortices. Specifically, at $Re \leqslant 3000$, the gap is occupied by a few larger-scale vortices in the bulk region along with some GV near the inner wall. As the Reynolds numbers is increased to $Re \geqslant 5000$, larger-scale vortices observed at smaller Re become severely distorted and break down into smaller vortices, in turn, the GV become closer to the wall. This finding is consistent with experimental observation of Baumert and Muller (Baumert & Muller 1995, 1997, 1999). In a wider gap (smaller radius ratio η) TC cell, in addition to large counter-rotating vortices spanning across the gap, Baumert and Muller also observed additional small and irregular vortices formed near the inner cylinder wall (Baumert & Muller 1999). The more prominent appearance of small-scale vortices near the inner wall with increasing curvature of the TC cell has also been confirmed by our DNS study of curvature-dependent viscoelastic turbulent TC flows (Song *et al.* 2019). Moreover, as pointed out in our previous study, these small-scale vortices are mainly generated through an elastic mechanism, as a result they have been dubbed 'elastic Görtler vortices'.

The existence of near-wall elastic GV and the effect of fluid inertia on their scales can be quantified via examination of the streamwise vorticity fluctuations $\omega'_{\theta\ rms}$ as depicted in figure 6. Specifically, all $\omega'_{\theta\ rms}$ profiles exhibit a local maximum and minimum in the inner-wall region. The near-wall quasi-streamwise vortices (QSV) model proposed by Kim, Moin & Moser (1987), ascribes the difference between the local minimum and maximum of $\omega'_{\theta\ rms}$ to the average intensity of the QSV that are generated as a consequence of a turbulent shear instability (Stone, Waleffe & Graham 2002; Li *et al.* 2006); the radial

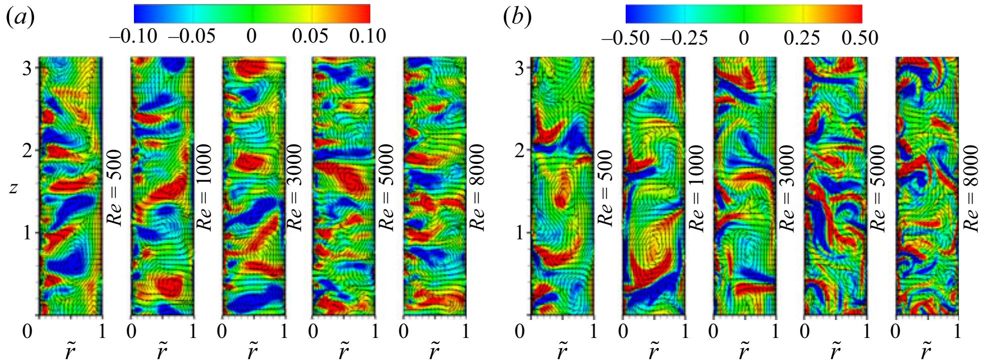

Figure 5. (a) Time and θ-direction averaged vectors of radial ($\langle u_r \rangle_{\theta,t}$) and axial ($\langle u_z \rangle_{\theta,t}$) velocities and contour plots of streamwise vorticity $\langle \omega_\theta \rangle_{\theta,t}$ in (r, z) plane; (b) instantaneous vectors of radial (u_r) and axial (u_z) velocities and contour plots of streamwise vorticity ω_θ in (r, z) plane with $\theta = \pi/2$ for various Re with $Wi = 30$.

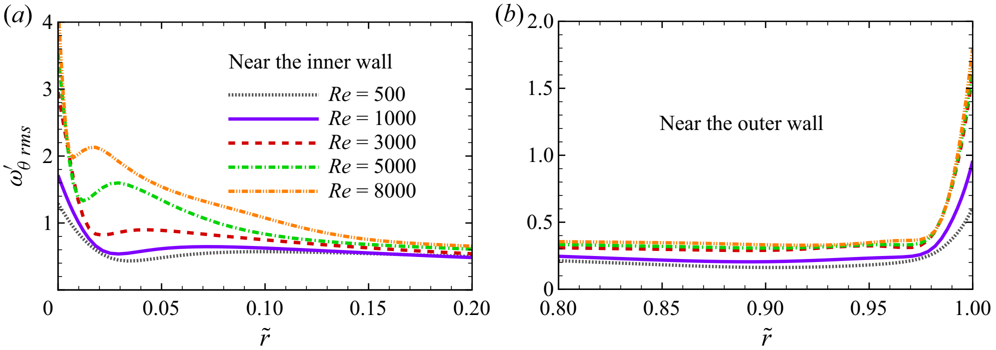

Figure 6. The r.m.s. values of azimuthal (streamwise) vorticity component for various Re with $Wi = 30$: (a) near the inner wall and (b) near the outer wall.

positions of the local minimum and maximum correspond to the average locations of the edge and centre of the QSV, respectively. Thus their distance is roughly proportional to the average size of the QSV. Near the inner wall, increasing Re makes the local maximum and minimum of $\omega'_{\theta\ rms}$ more pronounced (see figure 6a), consequently smaller size vortices appear as Re is increased (also see figure 7). Evidently, the small-scale GV become stronger in intensity and smaller in size with increasing Re, which indicates a gradual enhancement of the intensity of the turbulent shear instability in the inner-wall region. In contrast, vorticity fluctuations exhibit the opposite trend in polymer-induced drag reduction channel flows where near-wall QSV obtain an increase in size and a reduction in number and become highly elongated in the streamwise direction (Li *et al.* 2006; Kim *et al.* 2007; Xi & Graham 2012; Li *et al.* 2015; Teng *et al.* 2018). However, as shown in figures 5 and 6(b), small-scale GV are not observed in the outer-wall region for all Re considered here. This is in contrast to our earlier findings where slightly larger inertio-elastic GV formed near the outer cylinder wall (Liu & Khomami 2013b; Song *et al.* 2019). This points to the fact that the elastic effects needed to generate these inertio-elastic GV are not sufficient near the outer wall due to the smaller Wi and larger solvent to total viscosity ratio ($\beta = 0.9$) used in the present study.

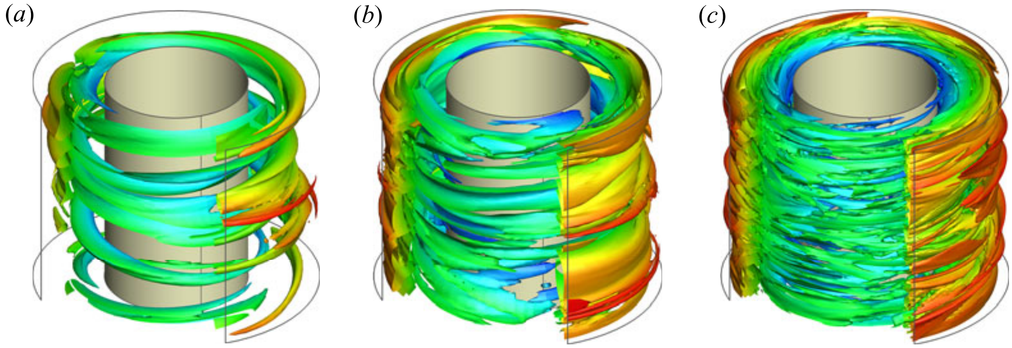

Figure 7. Instantaneous vortical structures visualized by Q-criterion with $Q = 0.001$ and coloured by the distance to the inner wall for the three main regimes of viscoelastic TC flow at (*a*) $Re = 500$, (*b*) $Re = 3000$, (*c*) $Re = 8000$, with $Wi = 30$. The flow structures in the region $\theta \in [3/2\pi, 2\pi]$ and $\tilde{r} \in [1/2, 1]$ are not shown to clearly display the small-scale vortical structures near the inner wall.

Although the small and irregular elastic GV formed near the inner cylinder wall have been observed in a series of prior experiments (Lee *et al.* 1995; Baumert & Muller 1995, 1997, 1999), the generation mechanism of these structures remains poorly understood due to the lack of polymer stress/body force measurements. To this end, a comparison of the production terms of the mean streamwise enstrophy budget equations (Dimitropoulos *et al.* 2001; Kim *et al.* 2007) near the inner wall is performed to shed light on the generation mechanism of the elastic GV. A detailed description of the budget equations for mean enstrophy is given in Appendix A. Here, we take the θ-component of the mean vorticity (W_θ) in (A3) and obtain the transport equation for mean streamwise enstrophy ($E_{\omega\theta} = W_\theta^2/2$). As seen in figure 8(*a*), the total streamwise enstrophy is balanced near the inner wall for $Re = 500$, demonstrating that a statistical steady state has been achieved. At $Re = 500$, $E_{\omega\theta}$ is mainly produced by the elastic effect T_ω that is almost balanced by viscous dissipation (ε_ω) since other typical shear production terms, i.e. production by mean (PM_ω) and fluctuating (PF_ω) strain of the mean vorticity as well as fluctuating enstrophy (FE_ω) are negligible. In addition, local balance (redistribution to opposite direction with equal magnitude) is achieved by two diffusive transports of the mean enstrophy, namely, by the solvent (DS_ω) and polymer (DT_ω) viscosity. The distributions of the main production terms with various Re are depicted in 8(*b*). Specifically, it is shown that the elastic production T_ω acts as the dominant source term for the $E_{\omega\theta}$ budgets as opposed to the typical shear term S_ω that is the sole generating mechanism for streamwise vortical structures in Newtonian TC flow. So, it is rational to label these near-inner-wall small-scale vortices as elastic GV (Song *et al.* 2019). However, increasing Re leads to a monotonic decrease of the dominant radial region of T_ω and a commensurate change in its position, i.e. it gets closer to the inner wall. This confirms that the decrease in size of these elastic GV discussed above indeed occurs by the redistribution of the streamwise vorticity fluctuations (see figure 6*a*). To this end, it is rational to expect that the entire gap will be filled with inertia-dominated vortical structures when Re gets much higher resulting in a gradual elimination of the elastic vortical structures.

It has been confirmed that the GV near the cylinder walls will cause near-wall streaky structures to form herringbone-like patterns in the Newtonian turbulent TC flows (Wei *et al.* 1992; Dong 2007). Similarly, as depicted in figure 9, herringbone-like patterns can also be observed from the spatial-temporal characteristics of the radial velocity near the inner wall in the inertio-elastic turbulent TC flows, especially at high Re. Evidently, it

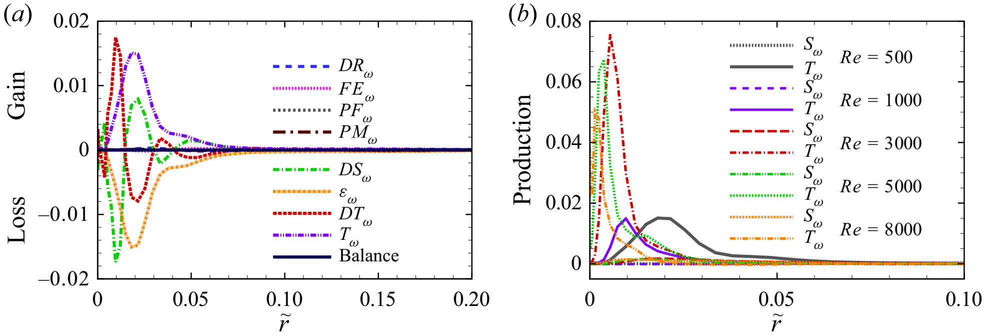

Figure 8. (*a*) Balance of mean streamwise enstrophy $E_{\omega\theta}$ of $Re = 500$, $Wi = 30$ near the inner cylinder wall. (*b*) Production terms of $E_{\omega\theta}$ for the viscoelastic TC flows for various Re with $Wi = 30$. Here, S_ω denotes the typical shear production including the mean and fluctuating strain as well as the fluctuating enstrophy, and T_ω represents the elastic production.

is the radial inflows and outflows at the boundaries of the counter-rotating elastic GV pairs that cause the streaky structures. Specifically, at $Re = 500$, only a few large and long herringbone streaks are distributed in disjoint bands around the outflow boundaries of the elastic GV and streaks from neighbouring bands barely intersect. As Re is increased, a considerable increase in the population of streaks is observed, and the spacing between neighbouring streaks is substantially decreased. Finally, at $Re = 8000$, the herringbone streaks become significantly finer and more closely packed, and their population is dramatically increased. However, the streaks become less coherent as evinced by their broken appearances, shorter lengths and scattered nature. The herringbone steaks in elastically dominated turbulent TC flows have sufficiently longer time life than their Newtonian counterparts due to their elastic origin. This is attributed to the fact that the fluid relaxation time (λ) governs this dynamical process in the elasticity-dominated regime. Consequently, increasing fluid inertia leads to a monotonic decrease in the lifetime of the herringbone steaks as a result of a significant reduction of elastic effects.

4. Polymer-induced turbulence dynamics

The flow structures discussed above (shown in figures 5, 7, 9) clearly demonstrate that the turbulent flow states are achieved for all Re considered. It should be noted that the Newtonian counterparts of $Re = 500$ and $Re = 1000$ are laminar flow states at radius ratio $\eta = 0.5$ (Dong 2007); thus the turbulence at $Re = 500$ and $Re = 1000$ is elasticity induced. As expected, in figure 10(*a*) the mean azimuthal velocity profiles obtain large radial gradients near both walls and an almost flat plateau in the bulk. The velocity gradient becomes larger and the flat region gets wider as the Reynolds number increases, suggesting an enhanced mean momentum transport in the wall regions and efficient mixing in the bulk due to the intense vortical circulations. Generally, the angular momentum ru_θ is the preferred variable to quantify the transport dynamics in a TC flow system, where the current of ru_θ is a conserved quantity that is transported from the inner to the outer cylinder (or *vice versa*) (Eckhardt, Grossmann & Lohse 2007). Instead of an essentially constant mean angular momentum of $0.5\Omega R_i^2$ observed in the bulk of Newtonian turbulent TC flow (Dong 2007), the mean angular momentum for the viscoelastic TC flow depicted in figure 10(*b*) is less than $0.5\Omega R_i^2$ and exhibits obvious

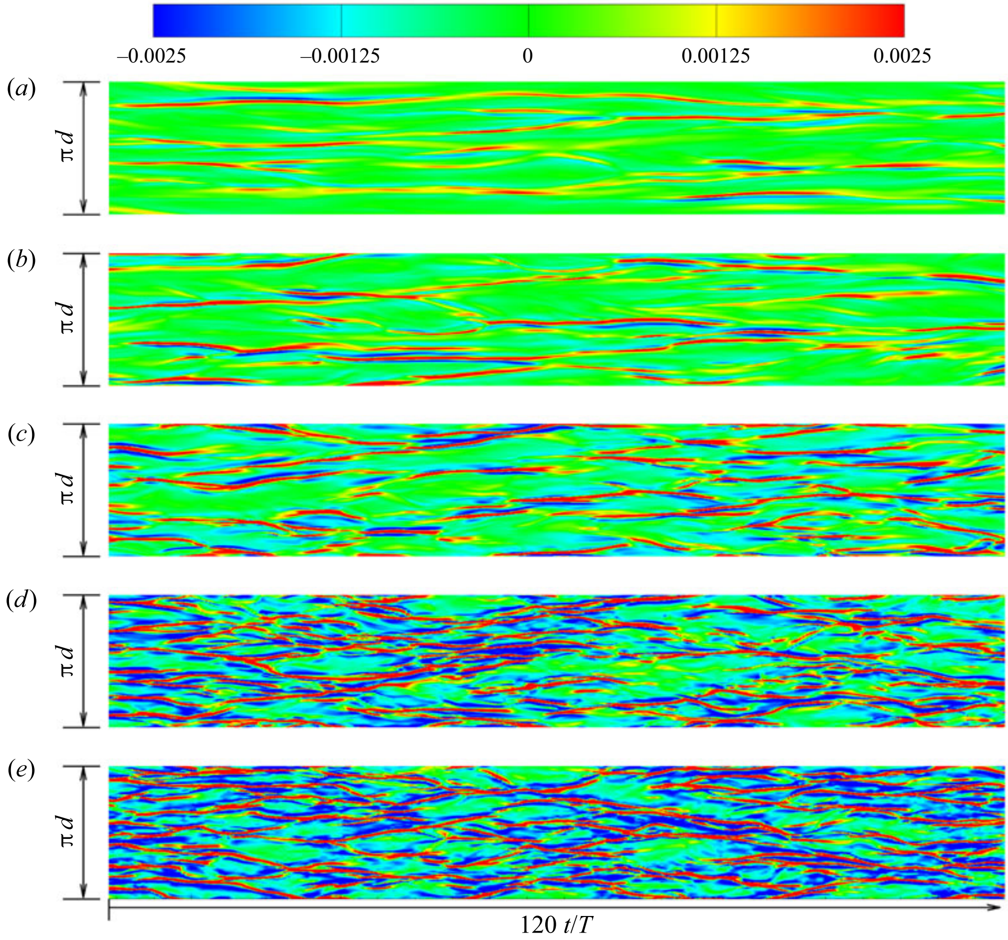

Figure 9. Space–time plots of radial velocity u_r along the axial line positioned at $\tilde{r} = 0.01$ and $\theta = \pi$ showing radial inflows (blue) and outflows (red) at (*a*) $Re = 500$, (*b*) $Re = 1000$, (*c*) $Re = 3000$, (*d*) $Re = 5000$, (*e*) $Re = 8000$, with $Wi = 30$.

positive gradients at the same *Re*; this indicates an efficient transport but an inefficient mixing of the mean angular momentum in the inertio-elastic turbulent TC flows.

For the viscoelastic turbulent TC flow, the same procedure used by Eckhardt *et al.* (2007) is applied to derive the angular momentum current J^{ω} as

$$J^{\omega} = r^3[\langle u_r\omega\rangle - \nu_s\partial_r\langle\omega\rangle - \nu_p\langle\tau_{r\theta}\rangle/r], \tag{4.1}$$

where ν_s and ν_p are dimensionless kinematic viscosities for solvent and polymers respectively, and $\nu_s = \beta/Re$, $\nu_p = (1-\beta)/Re$. The right-hand terms of (4.1) represent in sequence the convective flux (J^{ω}_c), the diffusive flux (J^{ω}_d) and the elastic source/sink term (J^{ω}_p) to angular momentum (Song *et al.* 2019). For a statistically stationary turbulent TC flow, the angular momentum current should be conserved (Eckhardt *et al.* 2007; Dong 2008), corresponding to a fact that the total torque exerted on the cylindrical fluid layers at a given radial position should be a r-independent constant (Van Gils *et al.* 2011). As expected, in figure 11, different yet constant values of the total angular momentum current are realized for all the viscoelastic TC flows. For all *Re* considered, the diffusive flux (J^{ω}_d)

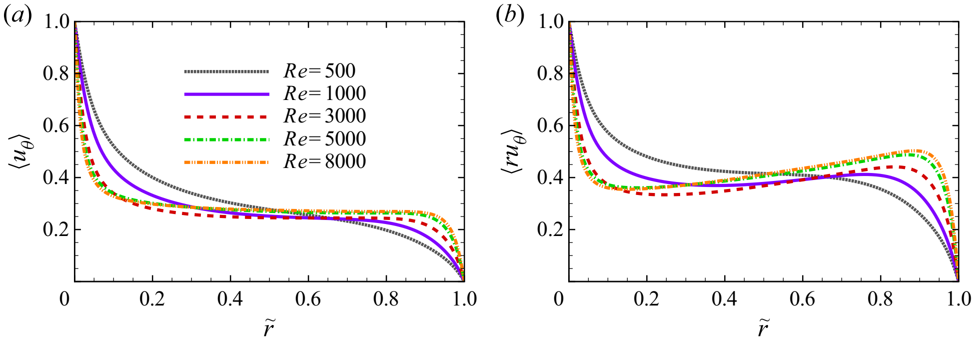

Figure 10. Profiles of (*a*) mean azimuthal velocity $\langle u_\theta \rangle$ and (*b*) mean angular momentum $\langle ru_\theta \rangle$ for various *Re* with $Wi = 30$.

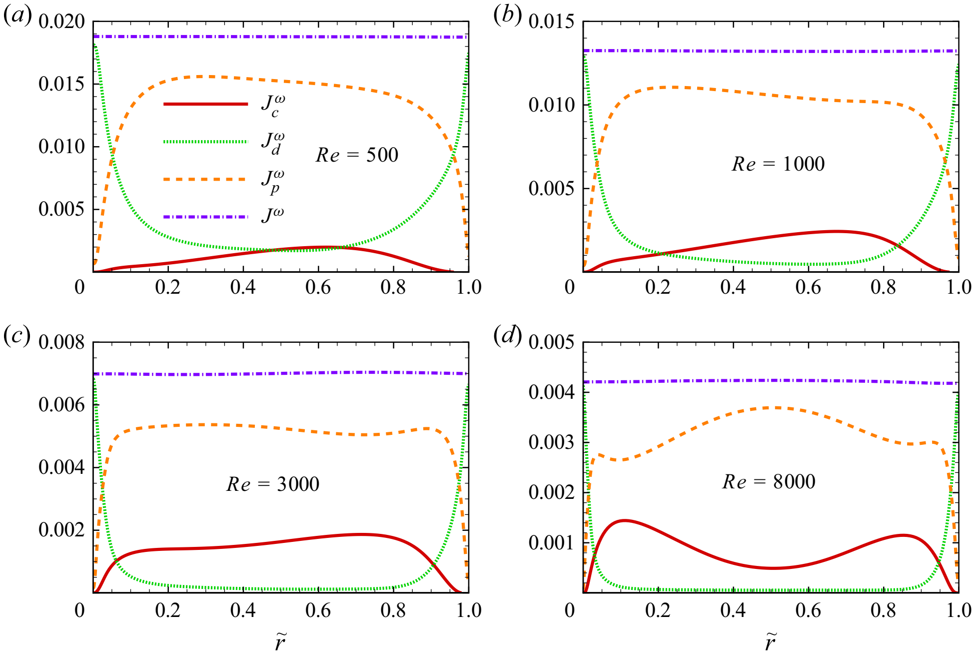

Figure 11. Balance of angular momentum current across the gap for viscoelastic TC flows of (*a*) $Re = 500$, (*b*) $Re = 1000$, (*c*) $Re = 3000$ and (*d*) $Re = 8000$, with $Wi = 30$.

has the dominant contribution to J^ω in the wall regions, while J_p^ω has the most significant contribution away from the walls (which is positive and thus a source term). However, with increasing *Re*, the convective flux (J_c^ω) gradually plays a more significant role in transport of the angular momentum in the bulk region. It should be noted that the diffusive flux (J_d^ω) makes a larger contribution than the convective flux (J_c^ω) in the entire gap at $Re = 500$, clearly demonstrating the negligible effect of convective flux in the flow (see figure 11*a*). The overall angular momentum current balance clearly underscores the fact that increasing the *Re* leads to a monotonic increase of the inertial contribution but a decrease of the elastic contribution to the J^ω-transport in the inertio-elastic TC flow.

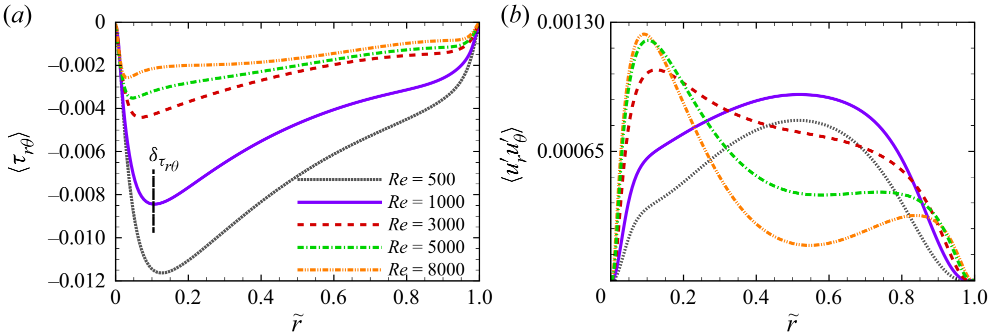

Figure 12. Mean polymer shear stress component $(1-\beta)\langle \tau_{r\theta} \rangle / Re$ (*a*) and Reynolds shear stress component $\langle u'_r u'_\theta \rangle$ (*b*) for various Re with $Wi = 30$. Here, $\delta_{\tau_{r\theta}}$ represents the thickness of boundary layer of $\langle \tau_{r\theta} \rangle$ for the inertio-elastic turbulent TC flows, defined as the distance from the inner wall to the radial position where the minimum of $\langle \tau_{r\theta} \rangle$ occurs.

As a consequence, near the inner wall the corresponding elastic shear stress (figure 12*a*) and inertial shear stress (figure 12*b*) both exhibit a monotonic increase with Re. Specifically, at all Re the mean elastic shear stress $\langle \tau_{r\theta} \rangle$ increases monotonically between its minimum in the inner-wall region and the local minimum of markedly higher value in the outer-wall region (see figure 12*a*). Elastic GV as expected (see figure 5*a*) enhance transverse momentum exchange and turbulent mixing of $\tau_{r\theta}$ via their vortical circulations. It should be noted that the minimum value of $\langle \tau_{r\theta} \rangle$ occurs close to the inner wall while the magnitude of this minimum decreases remarkably with increasing Re. Further, for each Re, a sharp decrease of $\langle \tau_{r\theta} \rangle$ in the inner-wall region indicates that the elastic GV have developed a $\langle \tau_{r\theta} \rangle$ boundary layer in the turbulent flow. Moreover, the radial position of the minimum of $\langle \tau_{r\theta} \rangle$ shifts slightly toward the inner wall for higher Re, leading to a further reduction of the polymer shear stress boundary layer thickness $\delta_{\tau_{r\theta}}$. In a turbulent TC flow, shear stress $\langle u'_r u'_\theta \rangle$ is mainly caused by the shear instability induced by the coupling of radial and azimuthal fluctuating motions that are generated by the vortical circulations (Bilson & Bremhorst 2007; Dong 2007). Specifically, the large-scale vortices in the bulk mainly generate the energetic radial fluctuating motions at the inflow/outflow vortex cell boundaries, while the small-scale vortices in the near-wall region are responsible for the intense azimuthal fluctuating motions. Hence, the distributions of inertial shear stress as shown in figure 12(*b*) clearly demonstrate a change from a regime dominated by large-scale centre-region vortices at low $Re \leqslant 1000$ to a small-scale near-wall vortices regime at high $Re \geqslant 5000$ (see figure 7). At the same time, the strong shear instability that results from these elastic GV causes a local maximum of $\langle u'_r u'_\theta \rangle$ for large Re. Moreover, for higher Re flows, a much higher inner-wall peak value of $\langle u'_r u'_\theta \rangle$ indicates a higher intensity of turbulent shear instability over the inner wall as compared with that over the outer wall.

The influence of Re on the inertio-elastic TC flows can also be quantitatively measured by comparing the power spectral density at various Re. The one-dimensional spectra of the TKE depicted in figure 13 capture approximately eight orders of magnitude of decay, indicating that the grid resolution is sufficient to cover the relevant spatial scales. For both the streamwise and the spanwise spectra, the small-scale values monotonically increase with Re and in the small-wavenumber (k) range the scaling of approximately $k^{-5/3}$ gradually appears. In EIT of channel flows, scaling law of $k^{-5/3}$ in the low-wavenumber range is also observed (Dubief *et al.* 2013). Generally, the Kolmogorov spectrum law of $-5/3$ is the hallmark of classical inertial turbulence. Thus, the progressive disappearance

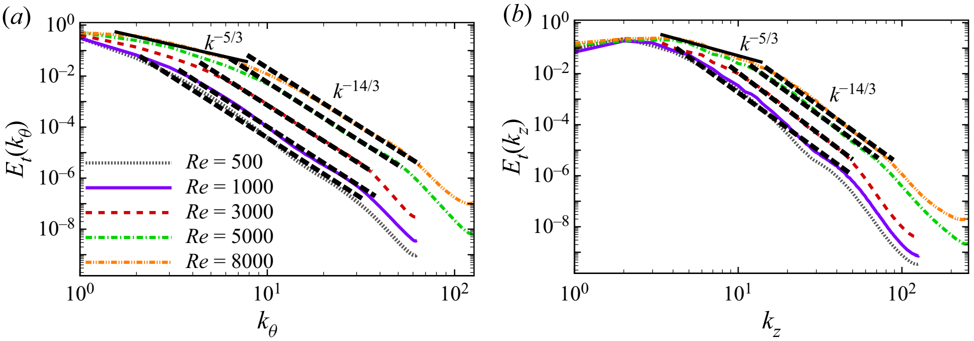

Figure 13. One-dimensional streamwise (*a*) and spanwise (*b*) spectra of the TKE ($\langle \boldsymbol{u}' \cdot \boldsymbol{u}' \rangle/2$) normalized by streamwise TKE ($\langle u'_\theta u'_\theta \rangle/2$) sampled at the middle of the gap for various Re with $Wi = 30$.

of the $-5/3$ scaling at large scales as Re is decreased, unequivocally demonstrates the gradual weakening of inertial effects on the flow. In fact, the scaling of velocity power spectra over a broad range of wavenumbers can be fitted by the power-law decay with the exponent of nearly $k^{-14/3}$, even at large Re. To this end, as Re is progressively decreased, the wavenumber range of the dissipation range progressively increases; correspondingly the wavenumber range where the power-law decay with the exponent of approximately $k^{-14/3}$ increases (see figure 13). Intriguingly, in the dissipation range the scaling with the exponent of nearly $k^{-14/3}$ is consistent with EIT in channel and decaying isotropic turbulent flows, where energy spectra often displays a scaling law of $k^{-\gamma}$ in the high-wavenumber range and γ is between 3.8 and 4.7 (Dubief *et al.* 2013; Watanabea & Gotoh 2013, 2014; Sid *et al.* 2018).

The polymer-induced changes in turbulence fluctuations can be ascertained via examination of energy exchange across the gap with a particular emphasis on the wall regions. To this end, the budgets of mean kinetic energy and TKE are analysed as they are good analytical tools to advance mechanistic understanding of complicated flow dynamics in wall-bounded turbulence (Dimitropoulos *et al.* 2001; Dallas & Vassilicos 2010; Thais, Gatski & Mompean 2012, 2013; Teng *et al.* 2018). The budget equations to quantify the energy cascade of viscoelastic turbulent TC flow are given below; the budget equation for the mean kinetic energy $E = \boldsymbol{U}^2/2$ is given by

$$\frac{\partial E}{\partial t} + \boldsymbol{U} \cdot \nabla E = \nabla \cdot (\underbrace{-P\boldsymbol{U}}_{D_{mp}} \underbrace{+2\nu_s \boldsymbol{U} \cdot \boldsymbol{S}}_{D_{ms}} \underbrace{+\nu_p \boldsymbol{U} \cdot \boldsymbol{T}}_{D_{me}} \underbrace{-\langle \boldsymbol{u}\boldsymbol{u} \rangle \cdot \boldsymbol{U}}_{D_{mt}}) \\ \underbrace{-2\nu_s (\nabla \boldsymbol{U}) : \boldsymbol{S}}_{\varepsilon_m} \underbrace{-\nu_p (\nabla \boldsymbol{U}) : \boldsymbol{T}}_{P_{me}} \underbrace{+\langle \boldsymbol{u}'\boldsymbol{u}' \rangle : (\nabla \boldsymbol{U})}_{P_t}, \tag{4.2}$$

and for the TKE $e = \langle \boldsymbol{u}' \cdot \boldsymbol{u}' \rangle/2$

$$\frac{\partial e}{\partial t} + \boldsymbol{U} \cdot \nabla e = \nabla \cdot (\underbrace{-\langle P'\boldsymbol{u}' \rangle}_{D_p} + \underbrace{2\nu_s \langle \boldsymbol{u}' \cdot \boldsymbol{s}' \rangle}_{D_s} + \underbrace{\nu_p \langle \boldsymbol{u}' \cdot \boldsymbol{\tau}' \rangle}_{D_e} - \underbrace{\langle \boldsymbol{u}'\boldsymbol{u}' \cdot \boldsymbol{u}' \rangle/2}_{D_t}) \\ \underbrace{-2\nu_s \langle (\nabla \boldsymbol{u}') : \boldsymbol{s}' \rangle}_{\varepsilon} \underbrace{-\nu_p \langle (\nabla \boldsymbol{u}') : \boldsymbol{\tau}' \rangle}_{P_e} \underbrace{-\langle \boldsymbol{u}'\boldsymbol{u}' \rangle : (\nabla \boldsymbol{U})}_{P_t}. \tag{4.3}$$

The mean strain rate and the fluctuating strain rate tensors are given by $\boldsymbol{S} = (\nabla \boldsymbol{U} + (\nabla \boldsymbol{U})^{\mathrm{T}})/2$ and $\boldsymbol{s}' = (\nabla \boldsymbol{u}' + (\nabla \boldsymbol{u}')^{\mathrm{T}})/2$, respectively. Specifically, in (4.2) and (4.3), the left side is merely the total time derivative of E or e following a mean-flow fluid particle, while the right side represents the various mechanisms that bring about changes in E or e. The first four divergence terms on right side are energy transport and redistribution caused by pressure (D_{mp}, D_p), viscous diffusion (D_{ms}, D_s), polymeric elastic stress (D_{me}, D_e) and turbulent stress (D_{mt}, D_t), respectively. When integrated over the entire gap, these terms will not contribute to the total budget. The fifth term represents the direct viscous dissipation of kinetic energy $(\varepsilon_m, \varepsilon)$ via its conversion into heat. It is important to emphasize that the sixth term represents the energy production associated with polymer stretch, which has been used to quantify energy exchange between kinetic and elastic energy, denoted as P_{me} and P_e, respectively. And the last term is turbulence shear production term P_t that arises due to interaction of the mean streamwise velocity gradient and Reynolds shear stress; P_t quantifies the loss of mean kinetic energy in (4.2), but the gain of TKE in (4.3).

The TKE budgets for Newtonian TC turbulence have been examined in detail by Bilson & Bremhorst (2007). Specifically, it is clearly shown how velocity fluctuations are produced, dissipated and transported across the gap. In what follows, the budget terms of key importance to the energy exchange processes are discussed. Of particular interest is the energy budget of EDT at $Re = 500$. Interestingly, the energy budgets terms at higher Reynolds numbers have a similar radial variation; however, the magnitude of each term has a large Re dependence.

As shown in figures 14(*a*) and 15(*a*), a total balance is obtained for the budget equations of the mean kinetic energy (E-budget) and TKE (e-budget) when a stationary steady turbulent state is realized. For the E-budget depicted in figure 14(*a*), the pressure and Reynolds stress transport terms, i.e. D_{mp} and D_{mt} are relatively small as compared with the viscous diffusion term D_{ms} and the polymeric diffusion term D_{me}. Here, D_{ms} acts to bring high-velocity fluids close to the walls, where D_{me} plays an important role in moving them away from the inner-wall vicinity. Dissipation term ε_m approaches its maximum value (acting as a loss) as the inner wall is approached, and in the inner-wall region it is balanced approximately by the viscous diffusion term D_{ms}. Additionally, the turbulent shear (P_t) and mean elastic potential energy (P_{me}) production terms are both negative across the entire gap, indicating the transformation of kinetic energy of mean flow to turbulent fluctuations and elastic potential energy associated with polymer stretch. Specifically, for all Re considered (see figure 14*b*), polymer chains extract energy across the entire gap from the mean flow via chain stretch. Moreover, P_{me} obtains a local minimum that corresponds to the radial position of the elastic GV at each Re; this minimum displays a monotonic increase with Re. Thus, increasing fluid inertia hinders the energy extraction process by which the mean elastic potential energy is generated. This also leads to a reduction of the magnitude of the mean polymer shear stress (see figure 12*a*).

The e-budget is illustrated in figure 15(*a*); the pressure term D_p and turbulent transport term D_t approximately mirror each other. Specifically, they alternate as gain and loss terms of relatively small magnitudes. The viscous and polymer diffusion terms, i.e. D_s and D_e transport the high-fluctuating velocity fluids close to the wall to the bulk region, and in turn the TKE is dissipated by the viscous dissipation term ε, particularly near the walls, and in turn it is extracted by the macromolecules via chain stretch term P_e in the bulk region. For the gain of e, the mean shear production term P_t has a maximum near the inner wall and a descending value away from the inner wall. However, the additional elastic production term P_e attains two local positive maximum values near the two walls that are much larger than the classical turbulent shear production term P_t. Thus, the turbulence generating mechanism in EDT is dominated by elastic effects.

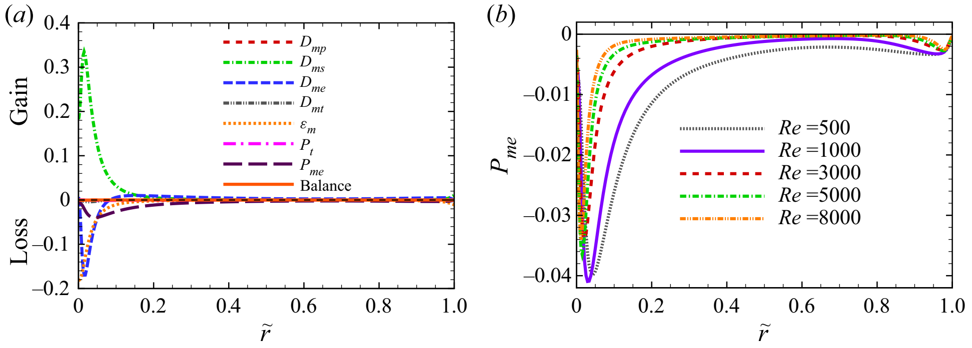

Figure 14. (*a*) Mean kinetic energy E-budget for viscoelastic TC flow of $Re = 500$, $Wi = 30$, (*b*) the elastic production P_{me} of E for various Re with $Wi = 30$.

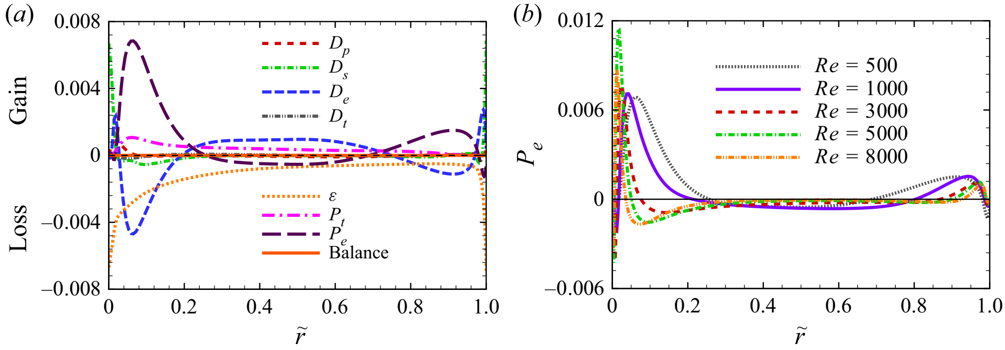

Figure 15. (*a*) TKE e-budget for viscoelastic TC flow of $Re = 500$, $Wi = 30$, (*b*) the elastic production P_e of e for various Re with $Wi = 30$.

The value of P_e is commonly used to quantify energy exchange between e and elastic potential energy $\epsilon = \nu_p(L^2 - 3)\langle \ln(f(\boldsymbol{C}))\rangle/2Wi$ (Dallas & Vassilicos 2010). Specifically, negative P_e means that the kinetic energy carried by fluctuating motions is absorbed and stored as elastic potential energy in stretched polymer chains; positive P_e means that elastic potential energy is released from the stretched polymer chains back to the turbulent flow. In fact, three energy exchange regions based on the sign of P_e, namely, the wall vicinity region with $P_e < 0$, the near-wall region with $P_e > 0$, and the core region with $P_e < 0$, have been identified in drag reduced or drag enhanced viscoelastic turbulent flows (Tsukahara *et al.* 2011; Teng *et al.* 2018; Zhu *et al.* 2020). As shown in figure 15(*b*), these three typical energy exchange regions are also observed in the present study. In fact, the second (positive P_e) region becomes smaller as Re is enhanced. The gradual disappearance of this second region implies that the turbulence derived from the elastic energy is inhibited by enhanced inertia. As a consequence, at high Reynolds number, $Re \geqslant 5000$, e is mainly produced by mean-flow shear production P_t (not show here), indicating an inertia-dominated global turbulence dynamics.

As a salient feature of EIT in pipe and channel flows, the markedly lower Reynolds shear stress than their Newtonian counterparts has been observed and interpreted as a qualitative result of the suppression of self-sustaining process of wall turbulence (Samanta *et al.* 2013; Choueiri *et al.* 2018; Lopez *et al.* 2019). However, the mechanism underlying the modification of $\langle u'_r u'_\theta \rangle$ by the elastic effect is still not well understood. To this end, budgets of the Reynolds shear stress $\langle u'_r u'_\theta \rangle$ are examined here with the aim of explaining how $\langle u'_r u'_\theta \rangle$ is produced, dissipated and transported across the gap. The equation describing the budget for $\langle u'_r u'_\theta \rangle$ is given as

$$\frac{\partial \langle u'_r u'_\theta \rangle}{\partial t} = P_{r\theta} + C_{r\theta} + TD_{r\theta} + PD_{r\theta} + PS_{r\theta} + D_{r\theta} + \varepsilon_{r\theta} + ED_{r\theta} + E_{r\theta}, \tag{4.4}$$

$$\left.\begin{aligned}
P_{r\theta} &= -\left(\langle u'_r u'_r \rangle \frac{\partial U_\theta}{\partial r} - \frac{U_\theta}{r} \langle u'_\theta u'_\theta \rangle \right), \quad C_{r\theta} = -\frac{U_\theta}{r}(\langle u'_r u'_r \rangle - \langle u'_\theta u'_\theta \rangle), \\
TD_{r\theta} &= -\frac{1}{r}\left[\frac{\partial (r \langle u'_r u'_r u'_\theta \rangle)}{\partial r} + \langle u'_r u'_r u'_\theta \rangle - \langle u'_\theta u'_\theta u'_\theta \rangle \right], \\
PD_{r\theta} &= -\left[\frac{1}{r} \frac{\partial (r \langle u'_\theta p' \rangle)}{\partial r} - \frac{2}{r} \langle u'_\theta p' \rangle \right], \quad PS_{r\theta} = \left\langle p' \left[\frac{1}{r}\left(\frac{\partial u'_r}{\partial \theta} - u'_\theta \right) + \frac{\partial u'_\theta}{\partial r} \right] \right\rangle, \\
D_{r\theta} &= \nu_s \left[\frac{1}{r} \frac{\partial (r \partial \langle u'_r u'_\theta \rangle / \partial r)}{\partial r} - \frac{4}{r^2} \langle u'_r u'_\theta \rangle \right], \\
\varepsilon_{r\theta} &= -2\nu_s \left[\left\langle \frac{\partial u'_r}{\partial r} \frac{\partial u'_\theta}{\partial r} \right\rangle + \frac{1}{r^2} \left\langle \left(\frac{\partial u'_r}{\partial \theta} - u'_\theta \right) \left(\frac{\partial u'_\theta}{\partial \theta} + u'_r \right) \right\rangle + \left\langle \frac{\partial u'_r}{\partial z} \frac{\partial u'_\theta}{\partial z} \right\rangle \right], \\
ED_{r\theta} &= \nu_p \left[\frac{\partial \langle \tau'_{rr} u'_\theta + \tau'_{r\theta} u'_r \rangle}{\partial r} + \frac{1}{r}(\langle \tau'_{rr} u'_\theta \rangle - 2\langle \tau'_{\theta\theta} u'_\theta \rangle + 3 \langle \tau'_{r\theta} u'_r \rangle) \right], \\
E_{r\theta} &= -\nu_p \left\{ \left\langle \tau'_{rr} \frac{\partial u'_\theta}{\partial r} \right\rangle + \left\langle \tau'_{r\theta} \frac{\partial u'_r}{\partial r} \right\rangle + \frac{1}{r} \left[\left\langle \tau'_{r\theta} \left(\frac{\partial u'_\theta}{\partial \theta} + u'_r \right) \right\rangle + \left\langle \tau'_{\theta\theta} \left(\frac{\partial u'_r}{\partial \theta} - u'_\theta \right) \right\rangle \right] \right. \\
&\quad \left. + \left\langle \tau'_{rz} \frac{\partial u'_\theta}{\partial z} \right\rangle + \left\langle \tau'_{\theta z} \frac{\partial u'_r}{\partial z} \right\rangle \right\},
\end{aligned}\right\} \tag{4.5}$$

where the terms on the right-hand side of (4.4) are the shear production ($P_{r\theta}$), the convection production ($C_{r\theta}$), the turbulence stress transport ($TD_{r\theta}$), the pressure diffusion ($PD_{r\theta}$), the pressure strain ($PS_{r\theta}$), the molecular diffusion ($D_{r\theta}$) and the dissipation ($\varepsilon_{r\theta}$). The last two terms are the polymer diffusion ($ED_{r\theta}$) and elastic production ($E_{r\theta}$) that are only present in viscoelastic flow. The budget terms in (4.5) are interpreted in the same manner as previously documented for Newtonian turbulent TC flow (Bilson & Bremhorst 2007).

As depicted in figure 16(*a*), the budget of the Reynolds stress $\langle u'_r u'_\theta \rangle$ is dominated by the production term $P_{r\theta}$, bulk gradient production term $C_{r\theta}$ and pressure terms ($PS_{r\theta}$, $PD_{r\theta}$) for inertio-elastic TC flow. In the entire gap, $\langle u'_r u'_\theta \rangle$ is mainly produced by $P_{r\theta}$ and $C_{r\theta}$. Other terms like the dissipation term $\varepsilon_{r\theta}$, viscous diffusion term $D_{r\theta}$ and turbulent transport term $TD_{r\theta}$ are non-zero, but substantially smaller in magnitude as also seen in Newtonian TC turbulence (Bilson & Bremhorst 2007). However, the polymer diffusion term $ED_{r\theta}$ plays an important role in moving the high-fluctuating stress to the inner-wall region, which in turn is absorbed by the elastic stress work ($E_{r\theta}$). As a consequence, in viscoelastic TC flows $\langle u'_r u'_\theta \rangle$ decreases mainly at the inner-wall region, while in the bulk region, $E_{r\theta}$ makes a positive contribution to the production of $\langle u'_r u'_\theta \rangle$. The *Re*-effects on the elastic work ($E_{r\theta}$) are illustrated in figure 16(*b*). Intriguingly, in the bulk and outer-wall vicinity, $E_{r\theta}$ has positive values. This indicates that the elastic work facilitates the production of turbulent shear stress especially at low Reynolds numbers, $Re \leqslant 1000$. In contrast, near the inner wall and slightly away from the outer wall, $E_{r\theta}$ has negative

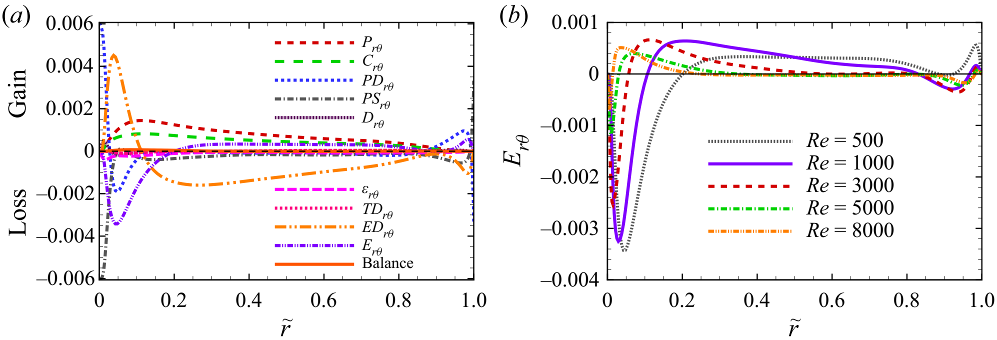

Figure 16. (*a*) Reynolds shear stress $\langle u'_r u'_\theta \rangle$-budget for viscoelastic TC flow of $Re = 500$, $Wi = 30$, (*b*) the elastic production $E_{r\theta}$ of $\langle u'_r u'_\theta \rangle$ for various Re with $Wi = 30$.

values; hence, elastic work acts to suppress the production of turbulent shear stress. Both the facilitation and suppression scenarios in modification of the Reynolds shear stress become less significant as Re is enhanced. This is consistent with the variation of $\langle u'_r u'_\theta \rangle$ shown in figure 12(*b*).

5. Flow–microstructure coupling

As discussed above, the most critical flow changes occur as a result of flow-induced polymer chain stretch in the wall regions. To address the details of polymer-induced flow–microstructure coupling, this section is devoted to examination of the polymer stretch/relaxation and the resulting polymeric elastic stress and body force that lead to flow modifications.

The extent of average polymer stretch can be quantified by the chain fractional extension ($\langle \mathrm{tr}(\boldsymbol{C}) \rangle / L^2$) defined as the ratio of the trace of the conformation tensor to the maximum polymer chain extensibility. As depicted in figure 17(*a*), for all Re considered, two local maxima of $\langle \mathrm{tr}(\boldsymbol{C}) \rangle / L^2$ are observed, one near the inner wall with the polymer chains almost fully stretched ($\langle \mathrm{tr}(\boldsymbol{C}) \rangle / L^2 \geqslant 80\,\%$) and another near the outer wall with relatively lower fractional extension. As Re is enhanced $\langle \mathrm{tr}(\boldsymbol{C}) \rangle / L^2$ increases almost in the entire gap, which is merely due to enhanced intensity of shear flow that results from the vortical circulations. However, the decrease in $\langle \mathrm{tr}(\boldsymbol{C}) \rangle / L^2$ as a function of radial position indicates that highly stretched polymer chains gradually relax as they are moved away from the inner-wall region. This observation is consistent with the fact that in drag reduced channel flows higher chain extension is realized in the near-wall region (Sureshkumar *et al.* 1997; Li *et al.* 2006; Kim *et al.* 2007; Samanta *et al.* 2013). As a consequence, the aforementioned polymer stretch leads to significant hoop stresses $\langle \tau_{\theta\theta} \rangle$ across the gap, see figure 17(*b*). Specifically, a higher $\langle \tau_{\theta\theta} \rangle$ is realized in the inner-wall region where a higher extension is realized. It is important to emphasize that an unstable stratification of the hoop stress is the prerequisite for the occurrence of solitary coherent structures like oscillatory strips and diwhirls in the elastically driven TC flows (Groisman & Steinberg 1997; Baumert & Muller 1999; Kumar & Graham 2000; Thomas *et al.* 2006*b*). As a consequence, the strong hoop stresses near the inner wall in inertio-elastic turbulent TC flow facilitate the generation of elastic GV structures (see figures 5, 7). Therefore, increasing fluid inertia hinders the hoop-stress generation, leading to a suppression for the elastic GV. Specifically, a sharp increase in $\langle \tau_{\theta\theta} \rangle$ is also observed in the inner wall region, indicating the existence of a inner-wall hoop-stress boundary layer $\delta_{\tau_{\theta\theta}}$ in the flow

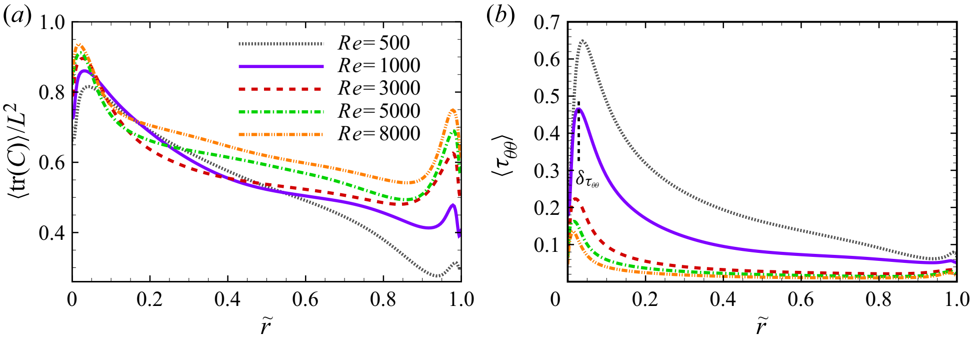

Figure 17. (*a*) Ensemble averaged chain fractional extension $\langle tr(\boldsymbol{C})\rangle/L^2$ and (*b*) mean hoop stress $(1-\beta)\langle\tau_{\theta\theta}\rangle/Re$ for various Re with $Wi = 30$. Here, $\delta_{\tau_{\theta\theta}}$ represents the thickness of boundary layer of $\langle\tau_{\theta\theta}\rangle$ for the inertio-elastic turbulent TC flows, defined as the distance from the inner wall to the radial position where the maximum of $\langle\tau_{\theta\theta}\rangle$ occurs.

(see figure 17*b*). The progressive thinning of the boundary layer $\delta_{\tau_{\theta\theta}}$ with Re confirms the suppressed role of the local elastic instability acting for the flow dynamics.

Generally, the role of hoop stress $\tau_{\theta\theta}$ in the viscoelastic TC flows can also be quantified by ascertaining its contribution to the radial polymer body force f_{pr} (Kumar & Graham 2000; Thomas *et al.* 2009; Liu & Khomami 2013*a*,*b*). Specifically, the radial polymer body force mainly results from the radial body force N_1/r and the radial stress gradient $\nu_p\langle\partial\tau_{rr}/\partial r\rangle$, where $N_1 = \nu_p\langle\tau_{rr} - \tau_{\theta\theta}\rangle$ is the first normal stress difference. As seen in figure 18(*a*), N_1/r is negative in the entire gap as $\langle\tau_{\theta\theta}\rangle$ is much greater than $\langle\tau_{rr}\rangle$ and N_1/r obtains a local minimum near the inner wall. Evidently, increasing Re leads to a monotonic decrease of the magnitude of N_1/r across the gap due to the weakening of hoop stresses (see figure 17*b*). As seen in figure 18(*b*), although the radial stress gradient obtains a positive value near the inner wall, f_{pr} is negative in the entire gap, even at the highest Re. Consequently, for all Re considered, this observation points to the fact that hoop stresses $\langle\tau_{\theta\theta}\rangle$ (via N_1/r) are the major contributor to the radial elastic body force and the main driving force for the elastic Görtler instability that occurs near the inner wall. In fact, in the inertio-elastic flow regime, the high fluctuations in polymer extension are closely associated with the small-scale elastic GV near the inner wall. Specifically, concentrated regions of high and low $\langle\mathrm{tr}(\boldsymbol{C})\rangle/L^2$ appear alternately along the inner and outer walls, and they are located at the centres of the inflow and outflow boundaries of adjacent counter-rotating vortex pairs (see figure 19*a*). At the inner wall, the regions of high $\langle\mathrm{tr}(\boldsymbol{C})\rangle/L^2$ are concentrated near the stagnation points of the radial outflow between two adjacent counter-rotating large-scale vortex cells (see figure 19*b*), where the outflow accelerates away from the inner wall and attains its maximum radial velocity (i.e. $\partial u_r/\partial r < 0$); hence, the incompressible fluid flow becomes transversely extensional. As a consequence, the substantially stretched polymer chains develop significant hoop stresses that trigger the elastic Görtler instability in this region leading to generation of a pair of elastic GV. It is well known that elastically driven solitary vortical structures such as oscillatory strips and diwhirls appear due to highly localized polymer extension in the radial inflow regions near the outer wall (Baumert & Muller 1997, 1999; Groisman & Steinberg 1997, 1998*a*; Kumar & Graham 2000; Thomas *et al.* 2006*a*, 2009). Conversely, the localized elastic GV structures in inertio-elastic turbulent TC flow result from the radial hoop stresses present near the inner cylinder.

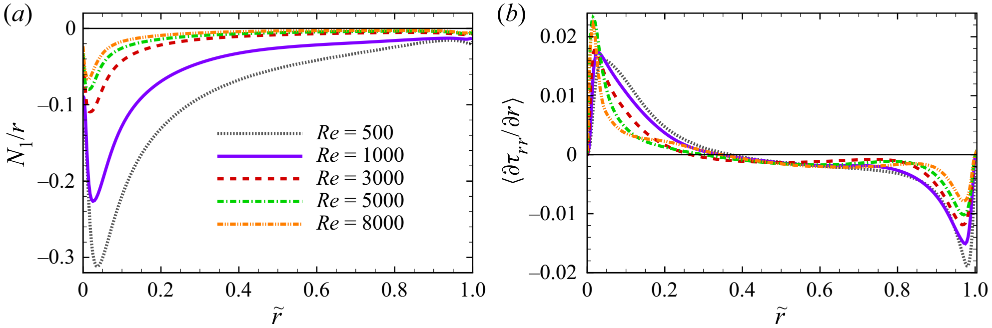

Figure 18. (*a*) Ensemble averaged radial body force N_1/r and (*b*) polymer radial stress gradient $(1-\beta)\langle\partial\tau_{rr}/\partial r\rangle/Re$ for various Re with $Wi = 30$. Where the first normal stress difference $N_1 = (1-\beta)\langle\tau_{rr}-\tau_{\theta\theta}\rangle/Re$.

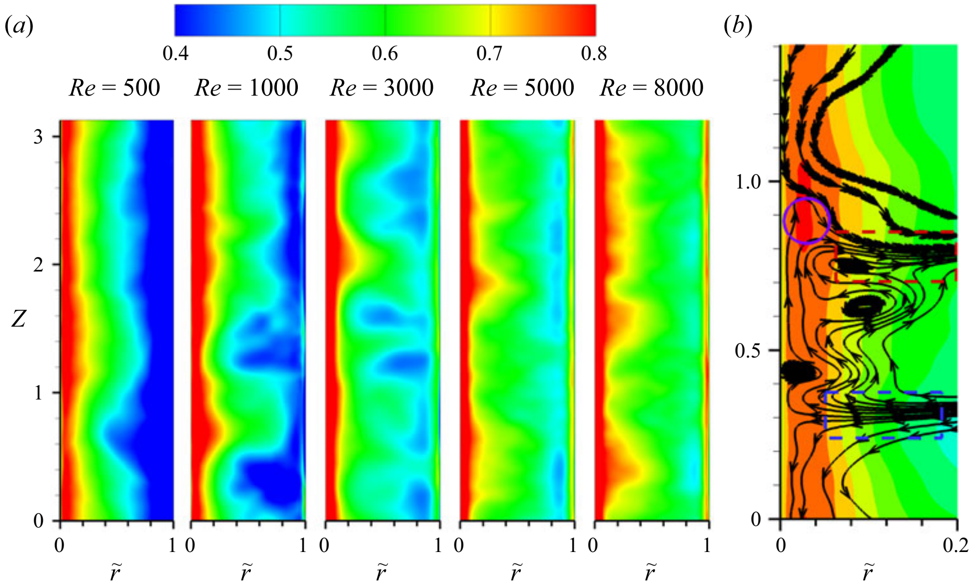

Figure 19. (*a*) Time and θ-direction averaged chain fractional extension $\langle\mathrm{tr}(\boldsymbol{C})\rangle/L^2$ in (r, z) plane for various Re with $Wi = 30$. (*b*) Magnified image of (*a*) for $Re = 3000$ near the inner wall. The (r, z) plane streamlines in (*b*) are plotted using the (u_r, u_z) velocities. Here, the purple circles are used to mark the localized regions with high polymer extension (the red regions of $\langle\mathrm{tr}(\boldsymbol{C})\rangle/L^2$ at the inner wall), the red dashed rectangle to mark the radial outflow ($u_r > 0$) region and blue dashed rectangle the radial inflow ($u_r < 0$) region.

6. Conclusions

In this work, high-fidelity three-dimensional DNS without use of AD has been performed to explore the influence of flow inertia on the inertio-elastic turbulent TC flows by varying the Reynolds number from 500 to 8000, corresponding to elasticity number of $0.00375 \sim 0.06$. It is found that increasing Re leads to a flow transition from an EDT to an IDT. Detailed statistical analysis demonstrates that the main contribution to transport and mixing of momentum, stress and energy comes from the large-scale flow structures in the bulk region for EDT, while the transport and mixing of physical quantities in IDT arise due to the small-scale flow structures in the near-wall regions. Nevertheless, the existence of small-scale elastic vortical structures identified as elastic GV has been observed for all *Re* considered and they tend to develop an elastic stress boundary layer near the inner wall, even for Reynolds numbers up to 8000. Moreover, it has been confirmed that the elastic GV are also able to develop herringbone streaks near the inner wall but with sufficiently longer time scale than their Newtonian counterparts due to their elastic origin. In addition, the polymer-induced flow–microstructure coupling analysis demonstrates that the elastic Görtler instability in the outflow regions of adjacent large-scale vortices where high polymer extension exists is triggered by significant hoop stresses. As a consequence, increasing fluid inertia hinders the hoop-stress generation, leading to a reduction in the size of the elastic GV.

The universal mechanism of the polymer–turbulence interaction is of great interest. This interaction can be quantified via the energy exchange between turbulent motions and mean flow and polymer chains. Specifically, the mean kinetic energy budget demonstrates that the polymer chains mainly absorb mean kinetic energy and convert it to mean elastic potential energy via mean-flow-driven chain stretch. The TKE budget demonstrates that the polymer absorbs TKE from the fluctuating motions near the wall and then releases it to the near-wall small-scale fluctuations to preserve the global dynamics. Furthermore, the Reynolds shear stress budget indicates that the elastic stress work has a negative contribution near the inner wall and slightly away from the outer wall; hence, it acts to suppress the production of turbulent shear stress. However, in the bulk and outer-wall vicinity, elastic stress work has a positive contribution that facilitates the production of turbulent shear stress. Generally, increasing fluid inertia hinders the generation of elastic stresses, leading to a monotonic depletion of the elastic-related nonlinear effects.

The EDT in TC flow displays differences as compared with EIT in the channel and pipe flows due to the persistence of large-scale vortical structures and the curvilinear streamline in TC flow. Evidently, EDT is dominated by the large-scale streamwise vortical structures while EIT is sustained by trains of spanwise-oriented flow structures with inclined sheets of stretched polymer chains. Despite these stark differences in the flow coherent structures, these two types of viscoelastic turbulence exhibit similarities in generation of turbulence and Reynolds stresses as well as energy spectrum scaling. Finally, in EDT of TC flow, the steep decay of energy spectra indicates a spatially smooth and temporally random flow reminiscent of ET. Therefore, the EDT flow state in the present study has provided much insight into the elastic stress-related statistical properties, turbulent dynamics as well as energy transfer between polymer chains and flow field of the ET flow state.

Acknowledgements. The calculations were completed on the supercomputing system in the Supercomputing Center of University of Science and Technology of China.

Funding. This work was supported by the National Natural Science Foundation of China (J.S., F.L., N.L. and X.-Y.L., grant number 12172353, 92052301, 91752110, 11621202, 11572312); and Science Challenge Project (N.L. and X.-Y.L., grant number TZ2016001); and National Science Foundation (B.K., grant number CBET0755269).

Declaration of interests. The authors report no conflict of interest.

Author ORCIDs.
Jiaxing Song https://orcid.org/0000-0002-9341-0345;
Fenghui Lin https://orcid.org/0000-0002-6909-0636;
Nansheng Liu https://orcid.org/0000-0001-9128-1933;
Xi-Yun Lu https://orcid.org/0000-0002-0737-6460;
Bamin Khomami https://orcid.org/0000-0002-0091-2312.

Appendix A. Derivations of mean enstrophy transport equations

The vorticity equation of incompressible viscoelastic fluid can be written as

$$\frac{\mathrm{D}\boldsymbol{\omega}}{\mathrm{D}t} = \boldsymbol{\omega}\cdot\nabla\boldsymbol{u} + \nu_s\nabla^2\boldsymbol{\omega} + \nu_p\nabla\times(\nabla\cdot\boldsymbol{\tau}), \tag{A1}$$

where $\boldsymbol{\omega} = \nabla\times\boldsymbol{u}$; ν_s and ν_p are the dimensionless kinematic viscosities for solvent and polymers, respectively, and $\nu_s = \beta/Re$, $\nu_p = (1-\beta)/Re$. The polymer stress tensor yields a supplementary contribution to the vorticity generation. Substituting the Reynolds decomposition $\boldsymbol{u} = \boldsymbol{U} + \boldsymbol{u}'$, $\boldsymbol{\omega} = \boldsymbol{W} + \boldsymbol{\omega}'$ and $\boldsymbol{\tau} = \boldsymbol{T} + \boldsymbol{\tau}'$ (where the capital letter denotes averaged variable, $\boldsymbol{U} = \langle\boldsymbol{u}\rangle$, $\boldsymbol{W} = \langle\boldsymbol{\omega}\rangle$, $\boldsymbol{T} = \langle\boldsymbol{\tau}\rangle$) into (A1) then averaging term by term, one obtains the mean vorticity equation

$$\frac{\mathrm{D}\boldsymbol{W}}{\mathrm{D}t} = \boldsymbol{W}\cdot\nabla\boldsymbol{U} + \langle\boldsymbol{\omega}'\cdot\nabla\boldsymbol{u}'\rangle - \langle\boldsymbol{u}'\cdot\nabla\boldsymbol{\omega}'\rangle + \nu_s\nabla^2\boldsymbol{W} + \nu_p\nabla\times(\nabla\cdot\boldsymbol{T}). \tag{A2}$$

The mean vorticity amplitude is defined as the mean enstrophy $\boldsymbol{E_\omega} = \boldsymbol{W}^2/2$. Dot product of the mean vorticity $\boldsymbol{W}$ and (A2) and commuting yields the following mean enstrophy transport equation

$$\begin{aligned}\frac{\mathrm{D}\boldsymbol{E_\omega}}{\mathrm{D}t} = \nabla\cdot(&\underbrace{\nu_s\nabla\boldsymbol{W}\cdot\boldsymbol{W}}_{DS_\omega}\underbrace{-\langle\boldsymbol{u}'\boldsymbol{\omega}'\rangle\cdot\boldsymbol{W}}_{DR_\omega}\underbrace{+\nu_p\nabla\times\boldsymbol{T}\cdot\boldsymbol{W}}_{DT_\omega})\underbrace{+(\boldsymbol{W}\cdot\nabla\boldsymbol{U})\cdot\boldsymbol{W}}_{PM_\omega}\\ &\underbrace{+\langle\boldsymbol{\omega}'\cdot\nabla\boldsymbol{u}'\rangle\cdot\boldsymbol{W}}_{PF_\omega}\underbrace{+\langle\boldsymbol{u}'\boldsymbol{\omega}'\rangle:\nabla\boldsymbol{W}}_{FE_\omega}\underbrace{-\nu_s\nabla\boldsymbol{W}:\nabla\boldsymbol{W}}_{\varepsilon_\omega}\underbrace{-\nu_p\nabla\times\boldsymbol{T}:\nabla\boldsymbol{W}}_{T_\omega}.\end{aligned} \tag{A3}$$

Specifically, the time rate of change of $\boldsymbol{E_\omega}$ following the mean flow is brought about by various mechanisms represented by the right-hand side of (A3). The first three divergence terms represent redistributed diffusion of mean enstrophy by solvent viscosity (DS_ω), and turbulence (DR_ω) and polymer stress (DT_ω). The fourth and fifth terms are the production by mean (PM_ω) and fluctuating (PF_ω) strain and stretch of the mean vorticity, respectively; FE_ω denotes the production of fluctuating enstrophy. The sum of these three generation terms are denoted as $S_\omega = PM_\omega + PF_\omega + FE_\omega$ due to their significance in Newtonian flows; ε_ω represents the direct solvent viscous dissipation of mean enstrophy. And the last term can be regarded as the elastic production by polymeric stress work marked as T_ω.

REFERENCES

AL-MUBAIYEDH, U.A., SURESHKUMAR, R. & KHOMAMI, B. 1999 Influence of energetics on the stability of viscoelastic Taylor–Couette flow. *Phys. Fluids* **11**, 3217–3226.

AL-MUBAIYEDH, U.A., SURESHKUMAR, R. & KHOMAMI, B. 2000 Linear stability of Taylor–Couette flow: influence of fluid rheology and energetics. *J. Rheol.* **44**, 1121–1138.

AL-MUBAIYEDH, U.A., SURESHKUMAR, R. & KHOMAMI, B. 2002 The effect of viscous heating on the stability of Taylor–Couette flow. *J. Fluid Mech.* **462**, 111–132.

ALVES, M.A., OLIVEIRA, P.J. & PINHO, F.T. 2021 Numerical methods for viscoelastic fluid flows. *Annu. Rev. Fluid Mech.* **53**, 509–541.

ANDERECK, C.D., LIU, S.S. & SWINNEY, H.L. 1986 Flow regimes in a circular Couette system with independently rotating cylinders. *J. Fluid Mech.* **164**, 155–183.

AVGOUSTI, M. & BERIS, A.N. 1993 Viscoelastic Taylor–Couette flow: bifurcation analysis in the presence of symmetries. *Proc. R. Soc. Lond.* A **443**, 17–37.

BARCILON, A. & BRINDLEY, J. 1984 Organized structures in turbulent Taylor–Couette flow. *J. Fluid Mech.* **143**, 429–68.

BARCILON, A., BRINDLEY, J., LESSEN, M. & MOBBS, P.R. 1979 Marginal instability in Taylor–Couette flows at a very high Taylor number. *J. Fluid Mech.* **94**, 453–68.

BAUMERT, B.M. & MULLER, S.J. 1995 Flow visualization of the elastic Taylor–Couette instability in Boger fluids. *Rheol. Acta* **34**, 147–159.

BAUMERT, B.M. & MULLER, S.J. 1997 Flow regimes in model viscoelastic fluids in a circular Couette system with independently rotating cylinders. *Phys. Fluids* **9**, 566–586.

BAUMERT, B.M. & MULLER, S.J. 1999 Axisymmetric and non-axisymmetric elastic and inertio-elastic instabilities in Taylor–Couette flow. *J. Non-Newtonian Fluid Mech.* **83**, 33–69.

BILSON, M. & BREMHORST, K. 2007 Direct numerical simulation of turbulent Taylor–Couette flow. *J. Fluid Mech.* **579**, 227–270.

BIRD, R.B., CURTISS, C.F., ARMSTRONG, R.C. & HASSAGER, O. 1987 Kinetic theory. In *Dynamics of Polymeric Fluids*, pp. 1397–1398. Wiley.

CHOSSAT, P. & IOOSS, G. 1994 Taylor vortices, spirals and ribbons. In *The Couette–Taylor Problem*, pp. 35–58. Springer.

CHOUEIRI, G.H., LOPEZ, J.M. & HOF, B. 2018 Exceeding the asymptotic limit of polymer drag reduction. *Phys. Rev. Lett.* **120**, 124501.

COLES, D. 1965 Transition in circular Couette flow. *J. Fluid Mech.* **21**, 385–425.

CRUMEYROLLE, O. & MUTABAZI, I. 2002 Experimental study of inertio-elastic Couette–Taylor instability modes in dilute and semidilute polymer solutions. *Phys. Fluids* **14**, 1681–1688.

DALLAS, V. & VASSILICOS, J.C. 2010 Strong polymer-turbulence interactions in viscoelastic turbulent channel flow. *Phys. Rev.* E **82**, 066303.

DIMITROPOULOS, C.D., SURESHKUMAR, R., BERIS, A.N. & HANDLER, R.A. 2001 Budgets of Reynolds stress, kinetic energy and streamwise enstrophy in viscoelastic turbulent channel flow. *Phys. Fluids* **13**, 1016–1027.

DONG, S. 2007 Direct numerical simulation of turbulent Taylor–Couette flow. *J. Fluid Mech.* **587**, 373–393.

DONG, S. 2008 Turbulent flow between counter–rotating concentric cylinders: a direct numerical simulation study. *J. Fluid Mech.* **615**, 371–399.

DUBIEF, Y., TERRAPON, V.E. & SORIA, J. 2013 On the mechanism of elasto-inertial turbulence. *Phys. Fluids* **25**, 110817.

DUBIEF, Y., TERRAPON, V.E., WHITE, C.M., SHAQFEH, E.S.G., MOIN, P. & LELE, S.K. 2005 New answers on the interaction between polymers and vortices in turbulent flows. *Flow Turbul. Combust.* **74**, 311–329.

DUTCHER, C.S. & MULLER, S.J. 2009*a* The effects of drag reducing polymers on flow stability: insights from the Taylor–Couette problem. *Korea-Aust. Rheol. J.* **21**, 223–233.

DUTCHER, C.S. & MULLER, S.J. 2009*b* Spatio-temporal mode dynamics and higher order transitions in high aspect ratio Newtonian Taylor–Couette flows. *J. Fluid Mech.* **641**, 85–113.

DUTCHER, C.S. & MULLER, S.J. 2011 Effects of weak elasticity on the stability of high Reynolds number co- and counter-rotating Taylor–Couette flows. *J. Rheol.* **55**, 1271–1295.

DUTCHER, C.S. & MULLER, S.J. 2013 Effects of moderate elasticity on the stability of co- and counter-rotating Taylor–Couette flows. *J. Rheol.* **57**, 791–812.

ECKHARDT, B., GROSSMANN, S. & LOHSE, D. 2007 Torque scaling in turbulent Taylor–Couette flow between independently rotating cylinders. *J. Fluid Mech.* **581**, 221–250.

FARDIN, M.A., PERGE, C. & TABERLET, N. 2014 'The hydrogen atom of fluid dynamics' – introduction to the Taylor–Couette flow for soft matter scientists. *Soft Matt.* **10**, 3523–3535.

FERNSTERMATCHER, P.R., SWINNEY, H.L. & GOLLUB, J.P. 1979 Dynamical instabilities and the transition to chaotic Taylor vortex flow. *J. Fluid Mech.* **94**, 103–128.

FOUXON, A. & LEBEDEV, V. 2003 Spectra of turbulence in dilute polymer solutions. *Phys. Fluids* **15**, 2060–2072.

GHANBARI, R. & KHOMAMI, B. 2014 The onset of purely elastic and thermo-elastic instabilities in Taylor–Couette flow: influence of gap ratio and fluid thermal sensitivity. *J. Non-Newtonian Fluid Mech.* **208–209**, 108–117.

GROISMAN, A. & STEINBERG, V. 1996 Couette–Taylor flow in a dilute polymer solution. *Phys. Rev. Lett.* **77**, 1480–1483.

GROISMAN, A. & STEINBERG, V. 1997 Solitary vortex pairs in viscoelastic Couette flow. *Phys. Rev. Lett.* **78**, 1460–1463.

GROISMAN, A. & STEINBERG, V. 1998*a* Elastic vs inertial instability in a polymer solution flow. *Europhys. Lett.* **43**, 165–170.

GROISMAN, A. & STEINBERG, V. 1998*b* Mechanism of elastic instability in Couette flow of polymer solutions: experiment. *Phys. Fluids* **10**, 2451–2463.

GROISMAN, A. & STEINBERG, V. 2000 Elastic turbulence in a polymer solution flow. *Nature* **405**, 53–55.

GROISMAN, A. & STEINBERG, V. 2004 Elastic turbulence in curvilinear flows of polymer solutions. *New J. Phys.* **6**, 29.

GROSSMANN, S., LOHSE, D. & SUN, C. 2016 High-Reynolds number Taylor–Couette turbulence. *Annu. Rev. Fluid Mech.* **48**, 53–80.

GUPTA, A. & VINCENZI, D. 2019 Effect of polymer-stress diffusion in the numerical simulation of elastic turbulence. *J. Fluid Mech.* **870**, 405–418.

HOUSIADAS, K.D. & BERIS, A.N. 2004 An efficient fully implicit spectral scheme for DNS of turbulent viscoelastic channel flow. *J. Non-Newtonian Fluid Mech.* **122**, 243–262.

HOUSIADAS, K.D., WANG, L. & BERIS, A.N. 2010 A new method preserving the positive definiteness of a second order tensor variable in flow simulations with application to viscoelastic turbulence. *Comput. Fluids* **39**, 225–241.

KIM, J., MOIN, P. & MOSER, R. 1987 Turbulence statistics in fully developed channel flow at low Reynolds number. *J. Fluid Mech.* **177**, 133–166.

KIM, K., LI, C.F., SURESHKUMAR, R., BALACHANDAR, S. & ADRIAN, R.J. 2007 Effects of polymer stresses on eddy structures in drag-reduced turbulent channel flow. *J. Fluid Mech.* **584**, 281–299.

KUMAR, K.A. & GRAHAM, M.D. 2000 Solitary coherent structures in viscoelastic shear flow: computation and mechanism. *Phys. Rev. Lett.* **85**, 4056–4059.

LARSON, R.G. 1992 Instabilities in viscoelastic flows. *Rheol. Acta* **31**, 213–263.

LARSON, R.G. & DESAI, P.S. 2015 Modeling the rheology of polymer melts and solutions. *Annu. Rev. Fluid Mech.* **47**, 47–65.

LARSON, R.G., SHAQFEH, E.S.G. & MULLER, S.J. 1990 A purely elastic transition in Taylor–Couette flow. *J. Fluid Mech.* **218**, 573–600.

LATRACHE, N., CRUMEYROLLE, O. & MUTABAZI, I. 2012 Transition to turbulence in a flow of a shear-thinning viscoelastic solution in a Taylor–Couette cell. *Phys. Rev.* E **86**, 056305.

LEE, S.H.K., SENGUPTA, S. & WEI, T. 1995 Effect of polymer additives on Görtler vortices in Taylor–Couette flow. *J. Fluid Mech.* **282**, 115–129.

LI, C.F., SURESHKUMAR, R. & KHOMAMI, B. 2006 Influence of rheological parameters on polymer induced turbulent drag reduction. *J. Non-Newtonian Fluid Mech.* **140**, 23–40.

LI, C.F., SURESHKUMAR, R. & KHOMAMI, B. 2015 Simple framework for understanding the universality of the maximum drag reduction asymptote in turbulent flow of polymer solutions. *Phys. Rev.* E **92**, 043014.

LIU, N.S. & KHOMAMI, B. 2013*a* Elastically induced turbulence in Taylor–Couette flow: direct numerical simulation and mechanistic insight. *J. Fluid Mech.* **737**, R4.

LIU, N.S. & KHOMAMI, B. 2013*b* Polymer-induced drag enhancement in turbulent Taylor–Couette flows: direct numerical simulations and mechanistic insight. *Phys. Rev. Lett.* **111**, 114501.

LOPEZ, J.M., CHOUEIRI, G.H. & HOF, B. 2019 Dynamics of viscoelastic pipe flow at low Reynolds numbers in the maximum drag reduction limit. *J. Fluid Mech.* **874**, 699–719.

LUMLEY, J.L. 1969 Drag reduction by additives. *Annu. Rev. Fluid Mech.* **1**, 367–384.

LUMLEY, J.L. 1977 Drag reduction in two phase and polymer flows. *Phys. Fluids* **20**, S64.

MARCHIOLI, C. & CAMPOLO, M. 2021 Drag reduction in turbulent flows by polymer and fiber additives. *KONA Powder Part J.* **38**, 64–81.

METZNER, A.B. 1977 Polymer solution and fiber suspension rheology and their relationship to turbulent drag reduction. *Phys. Fluids* **20**, S145.

MOHAMMADIGOUSHKI, H. & MULLER, S.J. 2017 Inertio-elastic instability in Taylor–Couette flow of a model wormlike micellar system. *J. Rheol.* **61**, 683–696.

MULLER, S.J. 2008 Elastically-influenced instabilities in Taylor–Couette and other flows with curved streamlines: a review. *Korea-Aust. Rheol. J.* **20**, 117–125.

OSTILLA-MÓNICO, R., VERZICCO, R. & LOHSE, D. 2015 Effects of the computational domain size on direct numerical simulations of Taylor–Couette turbulence with stationary outer cylinder. *Phys. Fluids* **27**, 025110.

SAMANTA, D., DUBIEF, Y., HOLZNER, M., SCHAFER, C., MOROZOV, A.N., WAGNER, C. & HOF, B. 2013 Elasto-inertial turbulence. *Proc. Natl Acad. Sci. USA* **110**, 12498.

SARIC, W.S. 1994 Görtler vortices. *Annu. Rev. Fluid Mech.* **26**, 379–409.

SHAQFEH, E.S.G. 1996 Purely elastic instabilities in viscometric flows. *Annu. Rev. Fluid Mech.* **28**, 129–185.

SHEKAR, A., MCMULLEN, R.M., MCKEON, B.J. & GRAHAM, M.D. 2020 Self-sustained elastoinertial Tollmien–Schlichting waves. *J. Fluid Mech.* **897**, A3.

SHEKAR, A., MCMULLEN, R.M., WANG, S., MCKEON, B.J. & GRAHAM, M.D. 2019 Critical-layer structures and mechanisms in elastoinertial turbulence. *Phys. Rev. Lett.* **122**, 124503.

SID, S., TERRAPON, V.E. & DUBIEF, Y. 2018 Two-dimensional dynamics of elasto-inertial turbulence and its role in polymer drag reduction. *Phys. Rev. Fluids* **3** (1), 011301.

SONG, J., TENG, H., LIU, N., DING, H., LU, X.-Y. & KHOMAMI, B. 2019 The correspondence between drag enhancement and vortical structures in turbulent Taylor–Couette flows with polymer additives: a study of curvature dependence. *J. Fluid Mech.* **881**, 602–616.

STEINBERG, V. 2019 Scaling relations in elastic turbulence. *Phys. Rev. Lett.* **123**, 234501–234505.

STEINBERG, V. 2021 Elastic turbulence: an experimental view on inertialess random flow. *Annu. Rev. Fluid Mech.* **53**, 27–58.

STONE, P.A., WALEFFE, F. & GRAHAM, M.D. 2002 Toward a structural understanding of turbulent drag reduction: nonlinear coherent states in viscoelastic shear flows. *Phys. Rev. Lett.* **89**, 208301.

SURESHKUMAR, R., BERIS, A.N. & AVGOUSTI, M. 1994 Non-axisymmetric subcritical bifurcations in viscoelastic Taylor–Couette flow. *Proc. R. Soc. Lond.* A **447**, 135–153.

SURESHKUMAR, R., BERIS, A.N. & AVGOUSTI, M. 1995 Effect of artificial stress diffusivity on the stability of numerical calculations and the dynamics of time-dependent viscoelastic flows. *J. Non-Newtonian Fluid Mech.* **60**, 53–80.

SURESHKUMAR, R., BERIS, A.N. & AVGOUSTI, M. 1997 Direct numerical simulation of the turbulent channel flow of a polymer solution. *Phys. Fluids* **9**, 743–755.

SWINNEY, H.L. & GOLLUB, J.P. 1985 Instabilities and transition in flow between concentric rotating cylinders. In *Hydrodynamic Instabilities and the Transition to Turbulence*, pp. 139–180. Springer.

TAKEDA, Y. 1999 Quasi-periodic state and transition to turbulence in a rotating Couette system. *J. Fluid Mech.* **389**, 81–99.

TALWAR, K.K., GANPULE, H.K. & KHOMAMI, B. 1994 A note on selection of spaces in computation of viscoelastic flows using the *hp*-finite element method. *J. Non-Newtonian Fluid Mech.* **52**, 293–307.

TAYLOR, G.I. 1923 Stability of a viscous liquid contained between two rotating cylinders. *Phil. Trans. R. Soc. Lond.* A **223**, 289.

TENG, H., LIU, N.S., LU, X.Y. & KHOMAMI, B. 2018 Turbulent drag reduction in plane Couette flow with polymer additives: a direct numerical simulation study. *J. Fluid Mech.* **846**, 482–507.

THAIS, L., GATSKI, T.B. & MOMPEAN, G. 2012 Some dynamical features of the turbulent flow of a viscoelastic fluid for reduced drag. *J. Turbul.* **13**, N19.

THAIS, L., GATSKI, T.B. & MOMPEAN, G. 2013 Analysis of polymer drag reduction mechanisms from energy budgets. *Intl J. Heat Fluid Flow* **43**, 52–61.

THOMAS, D.G. 2006 Flow instabilities and pattern formation in complex fluids: effect of elasticity and thermal gradients. PhD thesis, Washington University.

THOMAS, D.G., AL-MUBAIYEDH, U.A., SURESHKUMAR, R. & KHOMAMI, B. 2006*a* Time dependent simulations of non-axisymmetric patterns in Taylor–Couette flow of dilute polymer solutions. *J. Non-Newtonian Fluid Mech.* **138**, 111–133.

THOMAS, D.G., KHOMAMI, B. & SURESHKUMAR, R. 2006*b* Pattern formation in Taylor–Couette flow of dilute polymer solutions: dynamical simulations and mechanism. *Phys. Rev. Lett.* **97**, 054501.

THOMAS, D.G., KHOMAMI, B. & SURESHKUMAR, R. 2009 Nonlinear dynamics of viscoelastic Taylor–Couette flow: effect of elasticity on pattern selection, molecular conformation and drag. *J. Fluid Mech.* **620**, 353–382.

THOMAS, D.G., SURESHKUMAR, R. & KHOMAMI, B. 2003 Influence of fluid thermal sensitivity on the thermo-mechanical stability of the Taylor–Couette flow. *Phys. Fluids* **15**, 3308–3317.

TOMS, B.A. 1948 Some observations on the flow of linear polymer solutions through straight tubes at large Reynolds numbers. In *Proceedings of the First International Congress on Rheology* (ed. J.M. Burgers), pp. 135–141. North Holland.

TSUKAHARA, T., ISHIGAMIA, T., YUB, B. & KAWAGUCHIA, Y. 2011 DNS study on viscoelastic effect in drag-reduced turbulent channel flow. *J. Turbul.* **12**, 1–25.

VAITHIANATHAN, T. & COLLINS, L.R. 2003 Numerical approach to simulating turbulent flow of a viscoelastic polymer solution. *J. Comput. Phys.* **187**, 1–21.

VAITHIANATHAN, T., ROBERT, A., BRASSEUR, J.G. & COLLINS, L.R. 2006 An improved algorithm for simulating three-dimensional, viscoelastic turbulence. *J. Non-Newtonian Fluid Mech.* **140**, 3–22.

VAN GILS, D.P.M., HUISMAN, S.G., BRUGGERT, G.W., SUN, C. & LOHSE, D. 2011 Torque scaling in turbulent Taylor–Couette flow with co- and counterrotating cylinders. *Phys. Rev. Lett.* **106**, 024502.

VIRK, P.S. 1975 Drag reduction fundamentals. *AIChE J.* **21**, 625–656.

WATANABEA, T. & GOTOH, T. 2013 Hybrid Eulerian–Lagrangian simulations for polymer-turbulence interactions. *J. Fluid Mech.* **717**, 535–575.

WATANABEA, T. & GOTOH, T. 2014 Power-law spectra formed by stretching polymers in decaying isotropic turbulence. *Phys. Fluids* **26**, 035110.

WEI, T., KLINE, E.M., LEE, S.H.-K. & WOODRUFF, S. 1992 Görtler vortex formation at the inner cylinder in Taylor–Couette flow. *J. Fluid Mech.* **245**, 47–68.

WHITE, C.M. & MUNGAL, M.G. 2008 Mechanics and prediction of turbulent drag reduction with polymer additives. *Annu. Rev. Fluid Mech.* **40**, 235–256.

XI, L. & GRAHAM, M.D. 2012 Dynamics on the laminar-turbulent boundary and the origin of the maximum drag reduction asymptote. *Phys. Rev. Lett.* **108**, 028301.

YU, B. & KAWAGUCHI, Y. 2004 Direct numerical simulation of viscoelastic drag-reducing flow: a faithful finite difference method. *J. Non-Newtonian Fluid Mech.* **116**, 431–466.

ZHU, L. & XI, L. 2020 Inertia-driven and elastoinertial viscoelastic turbulent channel flow simulated with a hybrid pseudo-spectral/finite-difference numerical scheme. *J. Non-Newtonian Fluid Mech.* **286**, 104410.

ZHU, Y., SONG, J., LIU, N., LU, X. & KHOMAMI, B. 2020 Polymer-induced flow relaminarization and drag enhancement in spanwise-rotating plane Couette flow. *J. Fluid Mech.* **905**, A19.